

This work was written as part of one of the author's official duties as an Employee of the United States Government and is therefore a work of the United States Government. In accordance with 17 U.S.C. 105, no copyright protection is available for such works under U.S. Law.

Public Domain Mark 1.0

<https://creativecommons.org/publicdomain/mark/1.0/>

Access to this work was provided by the University of Maryland, Baltimore County (UMBC) ScholarWorks@UMBC digital repository on the Maryland Shared Open Access (MD-SOAR) platform.

Please provide feedback

Please support the ScholarWorks@UMBC repository by emailing scholarworks-group@umbc.edu and telling us what having access to this work means to you and why it's important to you. Thank you.



Technical Note: Constraining the hydroxyl (OH) radical in the tropics with satellite observations of its drivers: First steps toward assessing the feasibility of a global observation strategy

Daniel C. Anderson^{1,2}, Bryan N. Duncan², Julie M. Nicely^{2,3}, Junhua Liu^{2,4}, Sarah A. Strode^{2,4}, Melanie B. Follette-Cook⁵

1. GESTAR II, University of Maryland Baltimore County, Baltimore, MD, USA
2. Atmospheric Chemistry and Dynamics Laboratory, NASA Goddard Space Flight Center, Greenbelt, MD, USA
3. Earth System Science Interdisciplinary Center, University of Maryland, College Park, MD, USA
4. GESTAR II, Morgan State University, Baltimore, MD, USA
5. Mesoscale Atmospheric Processes Laboratory, NASA Goddard Space Flight Center, Greenbelt, MD, USA

Correspondence to: Daniel C. Anderson (daniel.c.anderson@nasa.gov)

Abstract

Despite its importance in controlling the abundance of methane (CH₄) and a myriad of other tropospheric species, the hydroxyl radical (OH) is poorly constrained due to its large spatial heterogeneity and the inability to measure tropospheric OH with satellites. Here, we present a methodology to infer tropospheric column OH (TCOH) in the tropics over the open oceans using a combination of a machine learning model, output from a simulation of the GEOS model, and satellite observations. Our overall goals are to assess the feasibility of our methodology, to identify potential limitations, and to suggest areas of improvement in the current observational network. The methodology reproduces the variability of TCOH from independent 3D model output and of observations from the Atmospheric Tomography mission (ATom). While the methodology also reproduces the magnitude of the 3D model validation set, the accuracy of the magnitude when applied to observations is uncertain because current observations are insufficient to fully evaluate the machine learning model. Despite large uncertainties in some of the satellite retrievals necessary to infer OH, particularly for NO₂ and HCHO, current satellite observations are of sufficient quality to apply the machine learning methodology, resulting in an error comparable to that of *in situ* OH observations. Finally, the methodology is not limited to a specific suite of satellite retrievals. Comparison of TCOH determined from two sets of retrievals does show, however, that systematic biases in NO₂, resulting both from retrieval algorithm and instrumental differences, lead to relative biases in the calculated TCOH. Further evaluation of NO₂ retrievals in the remote atmosphere is needed to determine their accuracy. With slight modifications, a similar methodology could likely be expanded to the extra-tropics and over land, with the benefits of increasing our understanding of the atmospheric oxidation capacity and, for instance, informing understanding of recent CH₄ trends.

1 Introduction

The hydroxyl radical (OH) dictates the lifetime of many tropospheric species, including carbon monoxide (CO), methane (CH₄), and numerous volatile organic compounds (VOCs). Knowledge of OH is therefore necessary to understand the abundance, distribution, and variability of these species. For instance, Rigby et al. (2017) and Laughner et al. (2021) attribute recent trends and increases in CH₄ at least partially to changes in OH abundance. Current constraints on OH are insufficient, however, to assess its relative importance in controlling these trends (Turner et al., 2017).



48 Differences in OH distributions among chemistry transport (CTM) and chemistry climate models (CCM)
49 suggest that these models are insufficient to inform understanding of OH abundance and variability
50 without further observational constraints. OH abundance can differ by up to 80% among models
51 constrained with identical emissions in intercomparison projects (Voulgarakis et al., 2013; Nicely et
52 al.; Zhao et al., 2019; Murray et al., 2021). Variables such as the photolysis frequency of O_3 (JO^1D) (Nicely
53 et al., 2020), the NO_x lifetime ($NO_x = NO + NO_2$), and the oxidation efficiency of VOCs (Murray et al.,
54 2021) contribute to these inter-model variations in OH. Likewise, the response of OH to the El Niño
55 Southern Oscillation (ENSO), the dominant mode of OH variability on monthly and seasonal timescales
56 (Anderson et al., 2021; Turner et al., 2018), and other modes of internal climate variability can vary
57 widely among models (Anderson et al., 2021).

58
59 Despite this need for better constraints, observations of tropospheric OH are limited. The hydroxyl
60 radical has a lifetime of approximately 1s (Mao et al., 2009), resulting in large spatial heterogeneity in
61 both the horizontal and vertical. A strategic, representative in situ observational network is therefore
62 unfeasible. As a result, observations of OH are generally limited to intensive field campaigns (Miller and
63 Brune, 2022) that have narrow spatial and temporal coverage. While remotely-sensed OH observations
64 are available, those from satellites are limited to the stratosphere (e.g., Pickett et al., 2008), while
65 ground-based observations of total column OH are dominated by the stratospheric contribution (e.g.,
66 Burnett and Minschwaner, 1998).

67
68 Reference gases with well-characterized sources and an OH sink, such as methyl chloroform (MCF), can
69 be used to infer OH abundance (Lovelock, 1977). This methodology, however, generally yields no
70 information on spatial heterogeneity beyond the hemispheric scale (e.g., Montzka et al., 2011; Rigby et
71 al., 2017; Naus et al., 2019). For MCF in particular, recent declines in tropospheric abundance will soon
72 dictate the need for a new reference species (Liang et al., 2017).

73
74 Multiple studies have attempted to constrain OH through the creation of proxies and the application of
75 satellite retrievals of OH drivers. Murray et al. (2014) showed that global OH strongly correlated with a
76 combination of JO^1D , water vapor ($H_2O_{(v)}$), and the tropospheric sources of reactive nitrogen and carbon
77 in the GEOS-Chem model. Murray et al. (2021) demonstrated that OH correlated with this proxy in
78 multiple CTMs, although the relationship differs strongly among models. Wolfe et al. (2019) developed
79 a proxy for OH based on formaldehyde (HCHO) production and loss rates. They applied that proxy to
80 satellite HCHO observations to estimate OH columns in the remote troposphere, a region where HCHO
81 abundance is low and the satellite retrievals are reflective of the *a priori* (Zhu et al., 2016). Using
82 machine learning, chemical transport model output, and retrievals of NO_2 and HCHO, Zhu et al. (2022a)
83 developed a method to estimate surface OH in North American urban areas. Finally, Pimlott et al.
84 (2022) used a steady state approximation of OH, including primary production from H_2O and O_3 and loss
85 from CO, CH_4 , and O_3 , to estimate OH between 600 and 700 hPa using observations from IASI (Infrared
86 Atmospheric Sounding Interferometer). A logical next step, building on the results of these studies, is
87 the development of a methodology to constrain OH that ingests multiple satellite retrievals,
88 encompasses the breadth of OH chemical and dynamical drivers, and spans a significant enough portion
89 of the globe to inform variability and trends in CH_4 and CO loss.

90
91 Combining machine learning, chemical transport model (CTM) output, and satellite data has the
92 potential to constrain tropospheric column OH (TCOH). A variety of machine learning techniques, such
93 as neural networks (Nicely et al., 2017; Nicely et al., 2020; Kelp et al., 2020), self-organizing maps
94 (Stauffer et al., 2016), random forest regression (Keller and Evans, 2019), and gradient boosted
95 regression trees (GBRTs) (Ivatt and Evans, 2020; Zhu et al., 2022a; Anderson et al., 2022) show promise in



helping to solve problems in atmospheric chemistry. In particular, Zhu et al. (2022a) and Anderson et al. (2022) demonstrated the ability of GBRTs to predict OH from a chemical transport model with reasonable accuracy. GBRT models (Elith et al., 2008; Chen and Guestrin, 2016) use an ensemble of decision trees to predict the value of a target based on multiple inputs, even for targets with highly non-linear dependencies on the inputs.

Here, we present a methodology to infer clear sky TCOH in the tropics from space-based observations of its chemical and dynamical drivers with the goal of assessing the feasibility of our methodology, identifying potential limitations, and suggesting areas of improvement in the current observational network. We train a GBRT model using output from a simulation of the NASA GEOS (Goddard Earth Observing System) model, and then estimate TCOH in the actual atmosphere at the satellite overpass time using inputs from a suite of satellite retrievals. In Section 2, we describe the methodology for generating the machine learning model as well as the satellite retrievals used to constrain TCOH. We then evaluate the suitability of MERRA2 GMI as a training dataset (Sect. 3) and, in Section 4, present a satellite-constrained OH product for one month from each season. Finally, in Section 5, we explore potential methodological limitations and benefits, including lack of validation data, the impacts of observational uncertainties, and the ability to use different satellites and retrievals as inputs to the GBRT model.

2 Description of the methodology to generate the GBRT model and of the associated datasets

Our overall aim is to demonstrate the feasibility of our approach to constrain TCOH with satellite-based observations over broad regional scales. As a first step, we restrict our analysis to latitudes equatorward of 25° and regions over water. We chose to focus initially on this domain as it has appreciable OH concentrations and simplified chemistry, as compared to regions with large biogenic and anthropogenic VOC emissions. Nevertheless, this portion of the atmosphere accounts for 50 – 60% of global CO and CH₄ loss. In this section, we describe the creation of the machine learning model used to predict TCOH (Sect. 2.1) for this region as well as the satellite products used as inputs to the machine learning model (Sect. 2.2).

2.1 Creation of the TCOH model

2.1.1 Creation of the GBRT training dataset

For the machine learning model training dataset, we use a subset of output from the MERRA2 GMI simulation (<https://acd-ext.gsfc.nasa.gov/Projects/GEOSCCM/MERRA2GMI/>). MERRA2 GMI is a 40 year (1980 – 2019) simulation of the NASA GEOS model run in replay mode (Orbe et al., 2017) with MERRA2 (Modern Era Retrospective analysis for Research and Applications, version 2) meteorology (Gelaro et al., 2017). The simulation has a resolution of c180 on the cubed sphere (approximately 0.625° longitude by 0.5° latitude) with 72 vertical layers and uses the Global Modeling Initiative (GMI) chemical mechanism (Duncan et al., 2007; Strahan et al., 2007). Output is available at daily- and monthly-averaged resolution, as well as instantaneous values corresponding with the overpass times of the satellites described in Section 2.2. Anderson et al. (2021) and Strode et al. (2019) provide detailed information about the simulation, including emissions.

The training target for the machine learning model is TCOH. In Anderson et al. (2022), we developed a GBRT parameterization trained on MERRA2 GMI output to predict in situ OH concentrations using 27 inputs, only a small fraction of which are observable from space. That parameterization, designed to be integrated into the GEOS modeling framework, performed better when there was a separate model for each month as opposed to one model for all months. While that GBRT model is not appropriate for the application described here, we employ a similar approach, creating a separate set of TCOH training



targets for each month. We use instantaneous OH output from MERRA2 GMI at 14:00 local time for each day of a given month across the years 2005 to 2019, to correspond with the satellite record. We omitted data from 2017 to evaluate model performance. For a given month and year, we calculate daily tropospheric column values across the grid, filtering out columns where the maximum cloud fraction in that column was greater than 30%, yielding approximately 43,000 valid grid boxes per day. For each year, we then average these values to monthly resolution. This results in approximately 600,000 total training targets for each month over the 15-year period.

151
 152
 153

Table 1: Input variables to the machine learning model and the corresponding satellite retrieval used to create the satellite OH product.

Variable	Satellite retrieval	Original horizontal and temporal resolution	Reference
Total O ₃ column	OMI TOMS-Like L3 version 3	0.25° × 0.25°, daily	McPeters et al. (2015)
Tropospheric NO ₂ column	OMI GSFC L3 version 4	0.25° × 0.25°, daily	Lamsal et al. (2021)
CO column	MOPITT L3 version 8	1.0° × 1.0°, monthly	Deeter et al. (2019)
HCHO column	OMI SAO L3 version 3	0.1° × 0.1°, daily	González Abad et al. (2015)
H ₂ O _(v) column	AIRS L3 version 6	1.0° × 1.0°, monthly	Susskind et al. (2014)
Sea surface temperature	MUR L4 version 4.2	0.25° × 0.25°, daily	Chin et al. (2017)
Aerosol optical depth at 550 nm	MODIS Aqua L3 collection 6	0.5° × 0.5°, daily	Levy et al. (2013)
H ₂ O _(v) layers: 925 – 850 hPa, 850 – 700 hPa, 700 – 600 hPa, 600 – 500 hPa, 500 – 400 hPa, 400 – 300 hPa, and 300 – 250 hPa	AIRS L3 version 6	1.0° × 1.0°, monthly	Susskind et al. (2014)
Solar zenith angle	N/A		
Latitude	N/A		

154

We selected the input variables for the machine learning model (Table 1) based on their relevance to OH chemistry and variability as well as our current ability to observe the variable with satellites. Performance was similar for a model including total column ozone only and for a model also including the tropospheric column. We therefore use total column ozone because of the uncertainties inherent in separating the column into two parts in the satellite retrieval. We chose the water vapor layers to correspond with the Atmospheric Infrared Sounder (AIRS) layers product. Layers are averages over the indicated pressure range, and we denote the layer names by the highest pressure in that range. We include sea surface temperatures (SST) as a proxy for the Indian Ocean Dipole and ENSO, which has a strong impact on OH variability in the tropics (Anderson et al., 2021; Turner et al., 2018). In addition, we include latitude and solar zenith angle as previous work has shown that these variables can explain a large fraction of the spatial OH variability (Duncan et al., 2000; Anderson et al., 2022).

156

We sampled the MERRA2 GMI output to create the training dataset in the same manner as for the TCOH targets. The inputs to the machine learning model each correspond to the same model column as the OH target. All column values are instantaneous and taken from 14:00 to correspond with satellite overpass times, except for CO, which is for 10:00, corresponding with the Measurement of Pollution in the Troposphere (MOPITT) overpass time. Model performance was similar when using CO output at 14:00 and 10:00, likely because of limited diurnal variability in CO column in the study region. SSTs are

167
 168
 169
 170
 171
 172



monthly averages of 24-hour averaged values, and we calculated solar zenith angle at the surface for noon on the 15th of a given month.

2.1.2 Creation and tuning of the GBRT model

We used the XGBoost package (Chen and Guestrin, 2016) version 0.81 in Python version 3.6 to create a GBRT model of TCOH for each month using the training datasets from MERRA2 GMI. For each month, we used 90% of the dataset for model training and the remainder for model validation. As mentioned in Section 2.1.1, we also used MERRA2 GMI output from 2017, which was omitted from the training dataset, as further validation.

To maximize parameterization performance while also balancing the potential of overfitting, we tuned hyperparameters, including the learning rate, the maximum tree depth, and the number of trees. We chose hyperparameter values that minimized the parameterization root mean square error (RMSE) of the training dataset. We set the learning rate, which controls the magnitude of change when adding a new tree, to 0.1, while we varied the maximum tree depth and number of trees from 6 to 22 and from 10 to 150, respectively. For both maximum tree depth and number of trees, RMSE initially dropped significantly with increasing value, representing sharp improvement in parameterization performance. RMSE values eventually plateaued, increasing parameterization runtime without noticeably improving performance. A combination of a maximum tree depth of 18 and 100 trees balanced performance with model training and run time.

To determine whether the inputs to the machine learning model improved or hindered performance, we performed a “leave one out” analysis. Using 5-fold cross validation, we retrained the model, individually omitting each of the inputs, to determine the percent difference between the mean RMSE of the 5 folds for the model without a specific input and one including all inputs. Omitting the inputs listed in Table 1 lead to increases in the RMSE, suggesting that each is necessary for improved model performance. As a result of this analysis, we do not use water vapor layers for pressures less than 300 hPa because these decreased model performance.

Finally, we found that it was not necessary to apply satellite averaging kernels and shape factors to the training dataset. Of the satellite retrievals used in this work (discussed in Sect. 2.2 and listed in Table 1), only CO, HCHO, and NO₂ could require convolving the model with the averaging kernel. Shape factors for the OMI NO₂ retrieval are determined from a similar setup of the GEOS model, also employing the GMI chemical mechanism and MERRA2 meteorology. Applying the satellite shape factors to the simulation discussed here would therefore not result in significant changes in the modeled NO₂ (Anderson et al., 2021). To test whether it is necessary to apply the averaging kernels for CO and HCHO, we created a separate training dataset, where we convolved the daily MERRA2 GMI output with the averaging kernel and a priori from the level 2 data for both species for February 2005 - 2019. All other inputs were kept the same. We then retrained the model with these adjusted CO and HCHO variables. When we applied the satellite data to the model for February 2017, as described in Section 4, the resulting TCOH differed by less than 1% on average from the model that did not include averaging kernel information. This level of uncertainty is significantly smaller than the other uncertainties discussed in Section 5, so we do not include averaging kernels in our analysis.

2.2 Description of satellite products

To create the observationally-constrained OH product, we use multiple satellite retrievals, listed in Table 1 and briefly described here. For each satellite retrieval, we use the level 3 gridded product, with the exception of SST which is level 4. Where necessary, we regridded the retrieval to a common horizontal



grid with a resolution of $1.0^\circ \times 1.0^\circ$ and averaged to the monthly scale. Each instrument is located onboard a polar orbiting satellite that provides near global coverage daily.

We use retrievals of three species – HCHO, O_3 , and NO_2 – from the Ozone Monitoring Instrument (OMI), an ultraviolet-visible spectrometer located onboard the Aura satellite, which has an overpass of approximately 13:30 local solar time (LST). We use the Smithsonian Astrophysical Observatory (SAO) version 3 HCHO retrieval (González Abad et al., 2015). Wolfe et al. (2019) found that this retrieval captured the variability of the HCHO columns in the remote atmosphere observed during the Atmospheric Tomography (ATom) campaign with little bias. For total column O_3 , we use the TOMS-like (Total Ozone Mapping Spectrometer) retrieval version 3 (McPeters et al., 2015), which agrees with ground-based and other satellite observations within approximately 1% (Labow et al., 2013). Finally, we use the Goddard Space Flight Center version 4 NO_2 retrieval (Lamsal et al., 2021). While previous studies have thoroughly evaluated this retrieval in more polluted atmospheres (e.g., Lamsal et al., 2014; Choi et al., 2020), evaluation in the remote tropical atmosphere, as defined in this study, is limited.

For water vapor and aerosol optical depth (AOD) at 550 nm, we use retrievals from AIRS and the Moderate Resolution Imaging Spectroradiometer (MODIS) instruments, respectively, both located onboard the Aqua satellite with an overpass of approximately 13:30 LST. We use the total column water vapor standard physical retrieval as well as the 7 water vapor layers listed in Table 1 (Susskind et al., 2014). Multiple studies have evaluated the accuracy of the AIRS $H_2O_{(v)}$ column and layers retrievals in the remote tropical atmosphere, finding bias of 5% or less and high correlation against both remote and *in situ* observations (Bedka et al., 2010; Anderson et al., 2016; Pérez-Ramírez et al., 2019). We use collection 6 of the dark target MODIS AOD retrieval at 550 nm, which is highly correlated with observations from the AERONET network over the ocean (Levy et al., 2013).

We also use retrievals of CO from MOPITT, which is onboard the Terra satellite with an overpass of 10:30 LST. We use the version 8 retrieval that includes both near and thermal infrared radiances (Deeter et al., 2019). CO retrievals from MOPITT in the remote tropics generally agree with ground-based remotely-sensed observations within 10% (Hedelius et al., 2019; Buchholz et al., 2017).

Finally, we use SSTs from the Multi-scale Ultra-high Resolution (MUR) analysis, which combines nighttime SST observations from multiple satellite platforms, including MODIS, as well as *in situ* observations and agrees with other SST analyses within $0.36^\circ C$ (Chin et al., 2017).

3 Evaluating the Suitability of the MERRA2 GMI Simulation as a Training Dataset

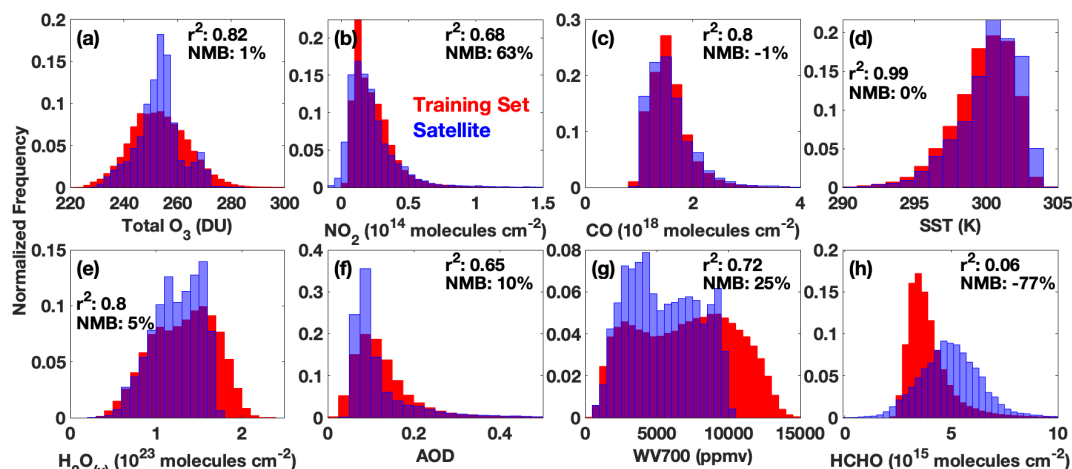
Before generating the GBRT model to predict TCOH, we first demonstrate that the MERRA2 GMI simulation is suitable to use as a training dataset. Because of the paucity of *in situ* observations of OH over most of the globe, we necessarily use output from an atmospheric chemistry model to train the machine learning model. The atmospheric chemistry model output must reasonably capture the distribution, magnitude, and ENSO-related variability of OH and the drivers listed in Table 1, as GBRT models are unable to extrapolate beyond the photochemical environments on which they are trained (Anderson et al., 2022).

3.1 Comparison of the Distribution and Magnitude of Simulated OH Drivers to Observations

Simulated OH from MERRA2 GMI agrees with observations over the remote ocean within the instrumental uncertainty. Anderson et al. (2021) compared MERRA2 GMI output to *in situ* observations from the first two deployments of the Atmospheric Tomography mission (ATom), finding modest correlation (r^2 values between 0.3 and 0.78 depending on the hemisphere and season) between



269 observations and the model. The average normalized mean bias was on the order of 20%, a slight high
 270 bias but within the 2σ observational uncertainty of 35%. Agreement was highest in the remote
 271 atmosphere, whereas the largest error was in regions of fresh, continental outflow off the coasts of
 272 South America and New Zealand.
 273



274 **Figure 1:** Comparison of the normalized distributions of the training dataset (red) for the February model and
 275 satellite observations of the indicated species for February 2017 (blue). Purple indicates regions of overlap. We
 276 use $H_2O_{(v)}$ at 700 hPa as an example for all $H_2O_{(v)}$ layers. Distributions of the other $H_2O_{(v)}$ layers are shown in Figure
 277 S1. We also indicate the r^2 of the correlation between MERRA2 GMI output for February 2017 and the
 278 corresponding satellite retrieval as well as the normalized mean bias of that output.
 279

280 The simulation captures both the observed variability and the magnitude of the majority of GBRT model
 281 inputs with reasonable fidelity, suggesting that the satellite retrievals highlighted in Section 2.2 are
 282 suitable inputs for a machine learning model trained on MERRA2 GMI output (Fig.1). Figure 1 compares
 283 the distribution of the February training dataset created from the MERRA2 GMI simulation for 2005 –
 284 2019 to the satellite observations of the indicated species for February 2017, a month omitted from the
 285 training dataset. Distributions of the remaining water vapor layers are shown in Figure S1. In addition,
 286 correlations between observations and MERRA2 GMI output for February 2017 are shown, as an
 287 example, in Figures S2 and S3. With the exception of HCHO, distributions of the species are similar
 288 between the observations and MERRA2 GMI, with the training dataset encompassing the full range of
 289 almost all species. A GBRT model trained on MERRA2 GMI will therefore likely not have to extrapolate
 290 to photochemical environments on which it was not trained when applied to the satellite data. Further,
 291 MERRA2 GMI total column O_3 , $H_2O_{(v)}$ column, AOD, CO, and SSTs are all highly correlated (r^2 of 0.65 or
 292 higher) with their respective satellite observations, and biases are within 10%, on average. Anderson et
 293 al. (2021) did show that MERRA2 GMI CO columns demonstrate biases of opposite sign in the Northern
 294 and Southern Hemispheres, however.
 295

296 Agreement between MERRA2 GMI and satellite observations for NO_2 , HCHO, and the $H_2O_{(v)}$ layers is
 297 more variable than for the other species. While modeled NO_2 is moderately correlated with
 298 observations ($r^2 = 0.68$) with relatively similar distributions, MERRA2 GMI has a NMB of 63%. This
 299 disagreement is most pronounced at low column values, however, where observational uncertainty is
 300 large. Further, Anderson et al. (2021) demonstrated distinct regions of bias in NO_2 related to biomass
 301 burning and lightning emissions. Modeled HCHO, on the other hand, is not correlated with observations



and is biased low by -77%. Modeled water vapor layers are all modestly correlated with observations (r^2 of 0.64 or greater) but vary in their bias, with the 925, 850, 700, and 300 hPa layers biased within 30% and the remaining layers biased up to 71%.

The satellite product is insensitive to the differences between the HCHO distribution of the satellite and training dataset highlighted in Figure 1. To determine the effects of the difference in HCHO distribution, we extended the training dataset to cover the full time period of the MERRA2 GMI simulation (1980 – 2019) and then subsampled the resultant data to match the satellite HCHO distribution. Extending the training dataset to 1980 allows for the subsampled training dataset to have a similar size (~600,000 points) as the original training set. We then created a new machine learning model using this subsampled dataset and calculated OH fields for Feb. 2017 using the satellite inputs from Table 1. We compared this to the TCOH field calculated from a model using the original training dataset, finding agreement within 5%. This uncertainty is small in comparison to that resulting from uncertainties in the NO_2 and HCHO satellite retrievals discussed in Section 5.2. If the uncertainty of the satellite inputs decreases, as retrievals and instruments improve, then it will become necessary to more closely align the training and observed HCHO distributions.

Finally, because NO_2 and HCHO have the largest differences between satellite observations and the training dataset, we trained a separate machine learning model to predict TCOH, omitting these two species as inputs. When this model was evaluated using the independent MERRA2 GMI output described in Section 4.1, the NRMSE was 10.1%, a more than factor of 2 degradation in performance as compared to the baseline model. This suggests that omitting these species from the machine learning model would result in a greater uncertainty in the final TCOH product than that which results from the retrieval uncertainties and the potential discrepancies between observations and the training dataset.

3.2 Evaluation of the simulated ENSO-related variability of OH drivers

Because ENSO is the dominant mode of OH variability (Anderson et al., 2021; Turner et al., 2018), the training dataset must also capture the ENSO-related variability of the GBRT model inputs. Anderson et al. (2021) demonstrated that the correlation of columns of CO, $\text{H}_2\text{O}_{(\text{v})}$, and to a lesser extent NO_2 , from the MERRA2 GMI simulation with the Multivariate ENSO Index (MEI) (Wolter and Timlin, 2011) agreed closely with correlations of the corresponding species for observations from MOPITT, AIRS, and OMI. Unsurprisingly, based on the strong correlation and low bias of MERRA2 GMI SSTs with observations, the simulation also captures the relationship between SSTs and ENSO. The simulation therefore sufficiently captures the ENSO-related variability of these species to act as training data for the GBRT model. We now evaluate this relationship for the remaining GBRT model inputs.

The MERRA2 GMI-simulated ENSO-related variability of AOD and the various water vapor layers also agrees well with observations. Figures 2 and S4 show the correlation of AOD, HCHO, and the various $\text{H}_2\text{O}_{(\text{v})}$ layers with the MEI for the satellite retrievals and MERRA2 GMI. MERRA2 GMI captures the general distribution and magnitude of correlation between AOD and ENSO, despite the low optical depths over much of the domain. There are some regional differences, however, particularly in the eastern Southern Hemispheric Pacific. For the $\text{H}_2\text{O}_{(\text{v})}$ layers, the simulation underestimates the magnitude of the correlation in some areas, but in general, there is excellent agreement for all layers throughout the troposphere. This suggests that, despite the high bias discussed above, including the $\text{H}_2\text{O}_{(\text{v})}$ layers could provide important, vertically-resolved information to the machine learning model.

Modeled accuracy of the HCHO-ENSO relationship is more difficult to assess. While both the OMI retrieval and MERRA2 GMI demonstrate broad regions of anti-correlation between HCHO and ENSO, the



correlations with OMI HCHO are weaker and noisier than for the other satellite retrievals. Over much of the domain, HCHO abundance is low, often at or below the retrieval detection limit, suggesting that the HCHO retrieval might not be of sufficient quality to capture ENSO-related variability. We investigate the impacts of the HCHO observational uncertainty in Section 5.

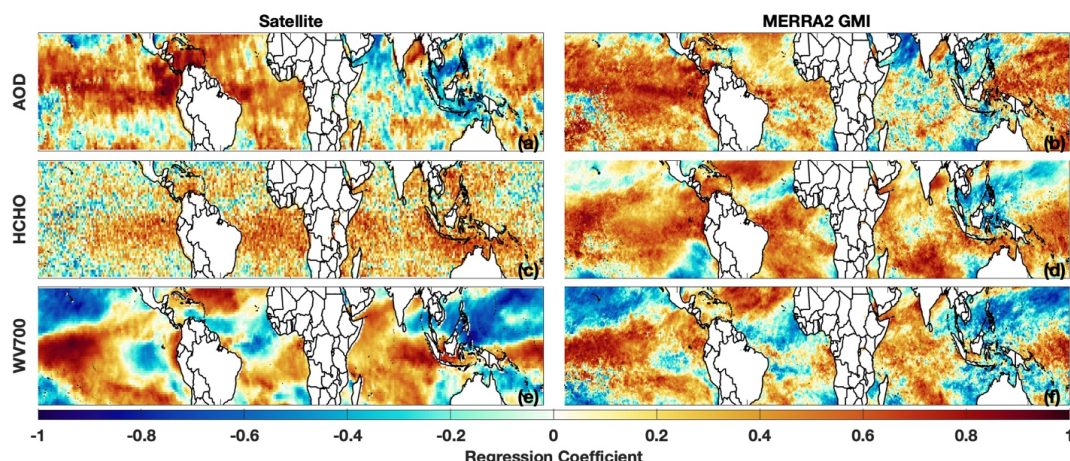


Figure 2: Distribution of the regression coefficient of a linear least squares fit of the indicated variable against the MEI for the respective satellite retrieval (a, c, and e) and MERRA2 GMI (b, d, and f) for February. Regressions of AOD are for 2010 to 2019, the years for which we have a one-degree, gridded satellite product, while HCHO and water vapor 700 hPa are for 2005 to 2019. Satellite data are on a $1^\circ \times 1^\circ$ grid while model output is at the native model resolution.

Finally, because we use total column O_3 as an input to the GBRT model, we do not evaluate the relationship between ENSO and O_3 , as the stratosphere dominates the O_3 column and the ENSO-related variability is mostly confined to the troposphere. Oman et al. (2013) found that a GEOS CCM simulation and a combination of O_3 retrievals from the Microwave Limb Sounder (MLS) and the Tropospheric Emission Spectrometer (TES) exhibited similar ENSO-related variability in the middle and upper troposphere, demonstrating that simulations in the GEOS framework can capture this relationship. If a TES-like satellite retrieval were currently available, it could be a valuable contributor to the GBRT model described here, as it would provide vertically-resolved information about one of the primary drivers of OH production.

4 Tropical tropospheric column OH constrained with observations of its drivers

We now demonstrate the ability of the GBRT model to determine TCOH. First, we show that the GBRT model can reproduce MERRA2 GMI modeled TCOH from a year independent of the training dataset, a so-called “hold out set” (Sect. 4.1). We then input satellite data from one month from each season into the GBRT model to evaluate the realism of the calculated TCOH fields (Sect 4.2).

4.1 Evaluation with an independent year from MERRA2 GMI

The machine learning model is able to capture both the magnitude and the variability of TCOH across each season when applied to MERRA2 GMI output from 2017, a year independent of the training dataset. For August 2017 (Fig. 3b), the predicted TCOH is highly correlated with MERRA2 GMI (r^2 of 0.98). TCOH from the machine learning model agrees with the CTM simulation within 4.8% on average. The overall normalized mean bias (NMB) is negligible (-0.1%), although there are some regions of



coherent bias (Fig. 3a). Results are similar for February, May, and October 2017 (Fig. S5). The normalized root mean square error for each of these months is comparable to that found for a GBRT parameterization of OH created with a similar methodology that included 27 inputs (Anderson et al., 2022). This suggests that limiting inputs to model variables observable from space does not degrade the ability of the machine learning model to predict TCOH. The low bias and high correlation between the GBRT and MERRA2 GMI TCOH for all four months examined here also suggests that any potential overfitting by the GBRT model is minimal.

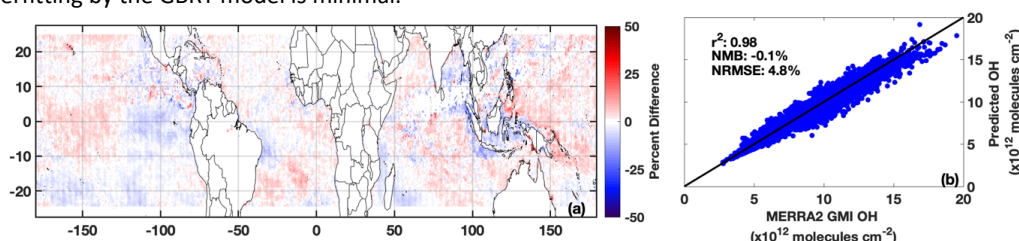


Figure 3: Percent difference between TCOH predicted by the machine learning model and that from MERRA2 GMI for August 2017, a month and year omitted from the training dataset (a). A regression of the machine learning TCOH against MERRA2 GMI for the same month (b). The r^2 of a linear, least squares regression, along with the normalized mean bias (NMB) and normalized root mean square error (NRMSE), are also indicated.

4.2 TCOH from satellite observations of its drivers

We now apply satellite data from the four months corresponding to the ATom campaign (Aug. 2016, Feb. 2017, Oct. 2017, and May 2018) to the GBRT model to determine TCOH fields across the tropics. More details about ATom as well as evaluation of the GBRT model with ATom observations are in Section 5. We use the satellite observations listed in Table 1, all of which have been averaged to the monthly scale and to a $1^\circ \times 1^\circ$ horizontal resolution. We include only grid boxes with observations for all GBRT model inputs and where those observations are within the range of the corresponding inputs from the training dataset. Because the satellite inputs for most species exclude grid boxes with a cloud fraction greater than approximately 30%, the product presented here represents predominantly clear sky conditions.

The GBRT model and multi-satellite inputs yield TCOH fields that are geophysically credible based on our current understanding of OH photochemistry. Although the domain-wide average changes little with season, with a minimum of 5.84×10^{12} molecules/cm² in May 2018 and a maximum of 6.35×10^{12} molecules/cm² in August 2016, the spatial distribution varies widely among the four months (Fig. 4). In both Feb. 2017 and Aug. 2016, TCOH minimizes in the winter hemisphere, consistent with lower OH production due to low insolation. The reverse is true for the summer hemisphere. In addition, TCOH maximizes in regions with strong continental outflow and along coastlines, regions likely to be impacted by anthropogenic and biomass burning emissions of OH drivers.

In general, TCOH from the multi-satellite product differs in both magnitude and distribution from the MERRA2 GMI simulation. For example, for Feb. 2017, mean MERRA2 GMI TCOH is 6.96×10^{12} molecules/cm², 12% higher than the satellite product (Fig. S6). This is consistent with the comparison to *in situ* observations discussed in Section 3.1 where MERRA2 GMI overestimates ATom observations by ~20% and underestimates CH₄ lifetime, suggesting that the satellite product is again of reasonable magnitude. While understanding the satellite/model differences is beyond the scope of this work, we consider the variety in TCOH spatial distributions generated by the GBRT model to be promising. The difference between the satellite-constrained product and MERRA2 GMI lends some confidence that the GBRT model is not overfit or “tied” to geographic determiners in the training dataset, but rather, is



sensitive to variations in the chemical and dynamical drivers of OH. These results all suggest that the methodology presented here can produce a reasonable satellite TCOH product in the tropics, with values and distributions independent of the chemistry model used to create the GBRT model.

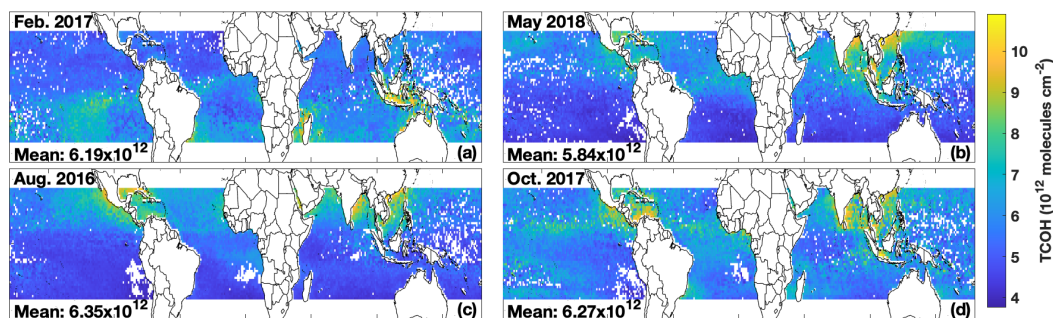


Figure 4: TCOH calculated with the machine learning model using satellite inputs for the months of each ATom deployment: Feb. 2017 (a), May 2018 (b), Aug. 2016 (c), and Oct. 2017 (d). The mean, domain-wide TCOH value in molecules/cm² for each month is also indicated.

5 Understanding and mitigating potential challenges in using this methodology to constrain TCOH

In this section, we outline possible limitations of the machine learning methodology and the current observational network of the GBRT model inputs and provide potential means to mitigate these limitations where necessary. In section 5.1, we discuss the current lack of sufficient in situ observations to thoroughly evaluate the methodology, highlighting this point by validating the GBRT model with data from the ATom campaign. In section 5.2, we investigate the impacts of random retrieval errors in satellite retrievals on the TCOH product, while in section 5.3, we evaluate the impacts on TCOH when using different satellite retrievals as inputs.

5.1 Insufficient in situ observations for thorough independent evaluation

While we demonstrated in Section 4.1 that TCOH calculated with the GBRT model agrees closely with a hold-out set from MERRA2 GMI, it is also important to demonstrate that the GBRT model can replicate observed TCOH from the actual atmosphere. Because the satellite TCOH product shown in Figure 4 is monthly and at a $1^\circ \times 1^\circ$ resolution, however, there are no observations with which to evaluate the product. We can test the ability of the GBRT model to reproduce observed TCOH from field campaigns, however, assuming there are concomitant observations of the input species listed in Table 1. The additional need for tropospheric column values of many of these species severely limits the datasets available for validation. To our knowledge, the ATom campaign is the only source of the required inputs with enough observations to attempt a limited validation.

During ATom (Thompson et al., 2022), scientists measured a suite of air quality and climate relevant trace gases and aerosols throughout the atmosphere above the remote Pacific and Atlantic. ATom took place in four parts: ATom 1 (July – August 2016), ATom 2 (January – February 2017), ATom 3 (September – October 2017), and ATom 4 (April – May 2018). During each deployment, flights consisted of a series of ascents and descents across all tropical latitudes over the Pacific and Atlantic Oceans. This allows for the calculation of tropospheric column content of the observed species and evaluation of the machine learning model across most latitudes of our study domain and across all seasons.

To evaluate the GBRT model performance, we calculated TCOH using the GBRT model and observations from the ATom deployments as inputs. We then compared the values to the observed OH columns. To



calculate the column values from the observations, we averaged data into 25 hPa pressure bins for each ATom profile. We filled in missing data using a log-linear interpolation and then integrated the column. Our analysis here includes only profiles with observations of all necessary species, that spanned at least 700 hPa, and where less than 25% of the pressure bin values were interpolated. We also omitted any profiles that had pressure bins with negative OH values. In addition, we restrict our analysis to latitudes within 25° of the equator and profiles conducted between 12:00 and 15:00 LST. Values for total column O_3 , AOD, and SSTs, for which there were no observations during ATom, were taken from the MERRA2 GMI simulation from the grid box closest to the center of the respective profile. The spatial distribution of the valid ATom columns and the corresponding columns calculated with the GBRT model are shown in Figure S7.

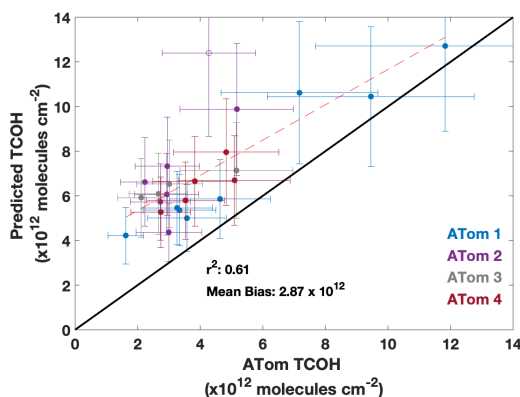


Figure 5: Regression of TCOH observed from the ATom deployments against that predicted from the GBRT model. Error bars represent the 2σ observational uncertainty as reported in Brune et al. (2020) and the GBRT uncertainty described in Section 5.2. The r^2 of a linear least squares fit and the mean bias is also shown.

The GBRT model captures the variability of the observed TCOH although there is a consistent high bias. When applied to all ATom deployments, predicted TCOH is correlated with the observations with an r^2 of 0.61 and a mean bias of 2.67×10^{12} molecules/cm² (Fig.5). Despite the high bias, many of the data points agree within the combined modeled and observational uncertainty. The r^2 value is heavily driven by one outlier from the ATom 2 campaign (open circle), which, when removed, increases the r^2 to 0.78. Likewise, there is variability in the correlation among the deployments, ranging from 0.94 for ATom 1 and 3 to 0.57 for ATom 2. The level of agreement between observed and predicted OH, particularly for ATom1 and 3, is comparable or better than that of other methods to infer OH from space. For example, Pimlott et al. (2022) found an r of 0.78 ($r^2 = 0.61$) when estimating ATom OH using a steady state approach, with r values ranging from 0.51 to 0.85 (r^2 of 0.26 to 0.72) for the different deployments. The level of agreement we show here therefore demonstrates the validity of the machine learning method to capture the variability of OH.

The source of the constant high bias, equal almost to a factor of 2 overestimate at the lowest column values, is unclear, although there are multiple potential error sources. For example, a typical profile taken during ATom spanned 300 – 400 km in latitude, disconnecting the top and bottom of the profile in space. This is in contrast to the data used to train the model, which were vertical columns over one location. This could lead to a degradation in model performance when applied to ATom, since the columns are not directly analogous to the training dataset. These effects are likely limited because ATom observations are in the remote atmosphere, where the spatial distribution of relevant species is



likely to be more homogeneous than over land. Likewise, in most cases, ATom columns do not span the entire troposphere. While this is unlikely to consistently result in large errors, if a large fraction of the tropospheric column of one input was outside the range of the ATom profile, this would likely cause large errors in calculated TCOH.

Further, there is a known interference with the ATom NO₂ observations. Because of thermal degradation of NO₂ reservoir species, such as organic nitrates and peroxyacetyl nitrate, in the instrument inlet, NO₂ observations are likely biased high (Shah et al., 2022; Thompson et al., 2022; Silvern et al., 2018). Recalculating the TCOH from ATom with NO₂ from a box model constrained with NO observations with a setup similar to that described in Nicely et al. (2016) yields a similar correlation (Fig. S8) as that shown in Figure 5 but with a lower slope, leading to underestimates at higher column values. The uncertainty in observed NO₂ could explain some of the scatter seen in Figure 5. For more certain evaluation with observations, greater certainty in the in situ NO₂ observations is needed. Although the in situ observations are insufficient to evaluate the absolute accuracy of the product, the results presented here demonstrate that a machine learning model trained on data from a CTM simulation can capture TCOH variability in the actual atmosphere.

5.2 Impacts of uncertainties in the satellite retrievals on TCOH

In the remote atmosphere where HCHO and NO₂ abundances are low, retrieval uncertainty of an individual pixel for both species can be on the order of 100% and is often reflective of the *a priori* (González Abad et al., 2015; Lamsal et al., 2021). Given the importance of these species to the GBRT model as well as to OH chemistry, it is necessary to determine how the propagation of the retrieval uncertainties from these and other model inputs impacts the predicted TCOH.

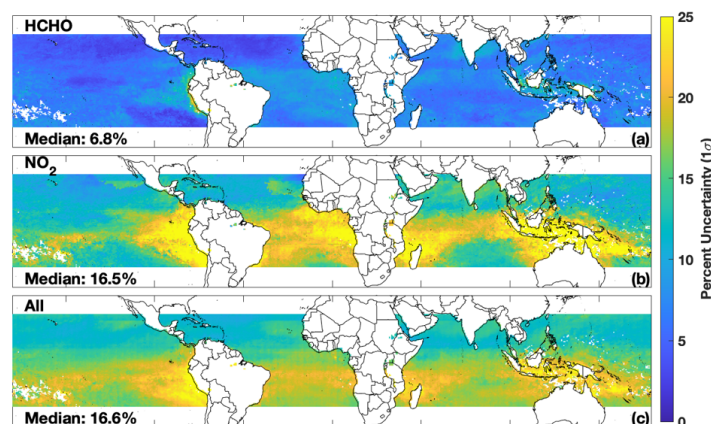
We determined the total uncertainty in TCOH from all inputs as well as the resultant uncertainty from each individual input for Feb. 2017. First, we estimated an average retrieval uncertainty for each input based on reported values in the retrieval files or from the literature (Table S1). We note that for NO₂ and HCHO we use a fit uncertainty for a single retrieval. Because we are using monthly-averaged data at 1° × 1° horizontal resolution, this likely significantly overestimates the actual uncertainty in these retrievals as the random error from individual pixels will tend to cancel when averaged over such large and spatial temporal scales. Our results are therefore an upper bound on the estimated TCOH uncertainty.

Next, for each grid box and model input, we created a Gaussian distribution of 2000 values with the modeled value for Feb. 2017 as the mean and the estimated uncertainty as the standard deviation. For each input, we then ran the GBRT model 2000 times to create a distribution of predicted TCOH values for each grid box. The normalized uncertainty in TCOH attributable to a given input is the ratio of the standard deviation of the resultant distribution divided by the mean value. We repeated this process individually for all inputs. In addition, to estimate a total uncertainty in TCOH, we varied all inputs simultaneously with the same Gaussian distributions described above.

Uncertainty from the NO₂ retrieval, and to a lesser extent HCHO, dominates the total uncertainty in the TCOH product but is of a magnitude comparable to that of in situ OH observations. Median TCOH 1σ uncertainty resulting from NO₂ is 16.5%, with maxima in the remote atmosphere in regions where NO₂ columns are low. Median uncertainty in TCOH resulting from HCHO is 7%, averaged over the study domain, despite the large uncertainty in the HCHO retrieval itself. In contrast to NO₂, uncertainties maximize in regions with higher HCHO columns (Fig. 6), although this is likely an overestimate as the retrieval uncertainty for these columns is lower than in the more remote atmosphere. In comparison,



545 median TCOH uncertainties resulting from other inputs are 2.9% or less (Figs. S9 and S10). Total TCOH
 546 uncertainty is 16.6% and is dominated by the NO₂ uncertainty.
 547



548 **Figure 6:** Normalized 1 σ uncertainty in the satellite TCOH product due to uncertainties in the HCHO (a) and NO₂
 549 (b) retrievals. The combined uncertainty from all input species is shown in panel c.
 550

551 These results demonstrate that the satellite retrieval inputs to the machine learning model are of
 552 sufficient quality to produce a meaningful TCOH data product when averaged over large spatial and
 553 temporal scales. The 2 σ uncertainty in TCOH resulting from the uncertainties in these retrievals is on
 554 the order of that reported for in situ OH observations (Brune et al., 2020). As discussed earlier, this is
 555 also likely an upper bound on the uncertainty from random retrieval errors, and uncertainties could be
 556 reduced through further averaging, although at the expense of reduced spatial and temporal resolution.
 557 Improving the satellite retrievals of NO₂ and HCHO in the remote atmosphere, using retrievals with less
 558 noise over the remote atmosphere such as HCHO from the Ozone Mapping and Profiler Suite (OMPS)
 559 (González Abad et al., 2016), or incorporating data from satellites with higher resolution, such as
 560 TROPOMI (Tropospheric Monitoring Instrument), could also reduce the uncertainty in their retrievals
 561 and thus in TCOH. As discussed in the next section, however, systematic biases between satellite
 562 retrievals can also lead to uncertainties in the TCOH.
 563

564 5.3 Sensitivity of TCOH to different satellite retrievals of GBRT inputs

565 The satellite retrievals listed in Table 1 provide the benefit of a long record, with data from most
 566 retrievals available from at least 2005 to the present. Such a rich dataset would allow for long-term
 567 trend analysis of TCOH. These instruments are near the end of their life cycle, however, so it is
 568 instructive to see how retrievals from newer satellites impact the predicted TCOH from the GBRT model.
 569 In addition, although these newer satellites, such as TROPOMI, have a significantly shorter observational
 570 record than those in Table 1, TROPOMI also has finer spatial resolution and the added advantage of
 571 providing retrievals for CO, NO₂, O₃, HCHO, and H₂O_(v). Using retrievals of multiple species from the
 572 same instrument could negate errors resulting from differences in viewing geometry as well as from
 573 overpass time. Here, we investigate the effects of applying retrievals from TROPOMI to the machine
 574 learning model and compare them to the results from the product described in Section 4, highlighting
 575 potential impacts resulting from instrumental differences as well as those resulting from differences in
 576 retrieval algorithms. The results emphasize the need for thorough retrieval validation in the remote
 577 atmosphere, particularly of NO₂.
 578



5.3.1 Description of TROPOMI

TROPOMI, a successor instrument to OMI, is a spectrometer covering portions of the ultraviolet, visible, and infrared spectrum (Veefkind et al., 2012). It is located onboard the Sentinel 5 Precursor satellite, which is polar orbiting and has a local overpass time of approximately 13:30. Horizontal resolution for the month examined here (May 2018) is $7 \text{ km} \times 3.5 \text{ km}$ at nadir. We have gridded the Level 2 product for each species to a $1^\circ \times 1^\circ$ resolution and averaged the data to the monthly scale, applying the recommended quality flags and filtering for cloud fraction greater than 30%.

We use two different retrievals of TROPOMI NO_2 for this analysis. First, we use the KNMI (Royal Netherlands Meteorological Institute) NO_2 retrieval (van Geffen et al., 2020), which is based on the DOMINO (Dutch OMI NO_2 product) retrieval developed for the OMI instrument. Wang et al. (2020) found that this retrieval was biased high when compared to ship-based observations from a MAX-DOAS instrument over the remote oceans. In addition, we use the MINDS (Multi-Decadal Nitrogen Dioxide and Derived Products from Satellites) retrieval, which uses the same algorithm as for the OMI product described in Section 2 (Lamsal et al., 2022). This retrieval has not been evaluated in the remote tropics.

We also use TROPOMI retrievals of HCHO , $\text{H}_2\text{O}_{(\text{v})}$, total column O_3 , and CO . The HCHO retrieval (De Smedt et al., 2018) was found to have a 30% low bias with respect to an OMI retrieval using the same algorithm due to differences in cloud processing (De Smedt et al., 2021). While evaluation in the remote tropics is limited, the TROPOMI retrieval does overestimate HCHO in polluted regions (De Smedt et al., 2021) when compared to ground-based observations. The TROPOMI $\text{H}_2\text{O}_{(\text{v})}$ (Chan et al., 2022) retrieval has a slight dry bias with comparison to other satellite products, while the total column O_3 retrieval (Garane et al., 2019) agrees within 0 – 1.5% with ground-based observations. Finally, the CO retrieval (Borsdorff et al., 2019) agrees with MOPITT over the oceans within 3% on average (Martínez-Alonso et al., 2020). TROPOMI does not have an equivalent retrieval of the AIRS $\text{H}_2\text{O}_{(\text{v})}$ layers.

5.3.2 TROPOMI data applied to the GBRT model

First, we calculate TCOH for May 2018 using inputs from TROPOMI. We trained a separate machine learning model using all inputs from Table 1 except the water vapor layers, for which there are no TROPOMI retrievals. Removal of the layers from the machine learning model does not significantly degrade performance. For example, for May 2017, removing the $\text{H}_2\text{O}_{(\text{v})}$ layers from the model, increases the NRMSE from 5.34% to 5.73% when applying the GBRT model to the hold out set. For this new model, we then calculate TCOH using TROPOMI data, including the KNMI NO_2 retrieval. For SSTs and AOD, we use the MUR and MODIS products respectively. While TROPOMI does have an aerosol product, the UV aerosol index, the corresponding output from the MERRA2 GMI simulation is unavailable. We refer to this as the TROPOMI-KNMI product. We have also calculated TCOH using the satellite retrievals in Table 1, except for the water vapor layers, using this GBRT model, and refer to that as the OMI/MOPITT/AIRS product.

TCOH from the TROPOMI-KNMI product are biased high with respect to those from the OMI/MOPITT/AIRS product. Figure 7 shows TCOH calculated from the TROPOMI-KNMI product as well as the percent difference between the two products. While there is modest correlation between the two ($r^2 = 0.63$), the TROPOMI product is 27.6% higher than the multi-satellite product, with overestimates across almost the entire domain. Differences between the products are most pronounced in the Indian Ocean and off the coasts of Indonesia and the Philippines.

In general, observations from TROPOMI agree with those from the satellites in Table 1, with the exception of NO_2 and HCHO . Ozone, $\text{H}_2\text{O}_{(\text{v})}$, and CO from TROPOMI are highly correlated (r^2 of 0.85 or



higher) with their respective retrievals from the OMI/MOPITT/AIRS product, with a modest high bias (less than 10%) in each case (Fig. S11). Note that we do not seek to identify the more accurate retrievals here; we are reporting the bias with respect to the satellite products listed in Table 1 because those retrievals underlie the TCOH product. TROPOMI NO₂ and HCHO, on the other hand, are systematically biased with respect to their respective OMI products, with a distinct high bias in KNMI-NO₂ (145%) and low bias in HCHO (20%). The higher TCOH from the TROPOMI product is consistent with the increase in NO₂, which would lead to higher secondary production of OH. Further, while TROPOMI KNMI-NO₂ is modestly correlated with OMI NO₂ ($r^2 = 0.61$), TROPOMI and OMI HCHO are not correlated ($r^2 = 0.23$), highlighting the difficulty of the HCHO retrieval.

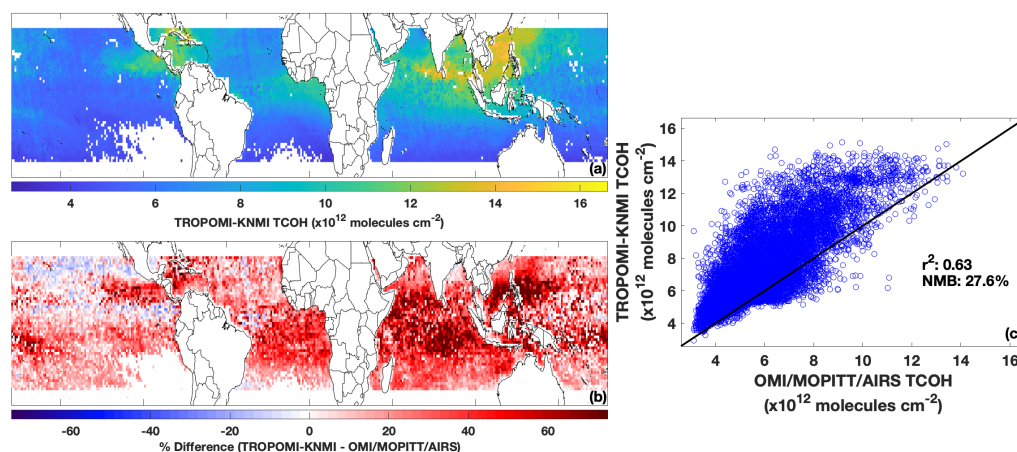


Figure 7: TCOH for May 2018 determined using TROPOMI inputs, including the KNMI NO₂ retrieval (a). The difference between the TROPOMI and multi-satellite product is shown in (b). Panel (c) shows the regression of TCOH calculated from TROPOMI against that calculated from retrievals from MOPITT, OMI, and AIRS.

NO₂ drives the differences between the two TCOH products. To determine the impacts of the different TROPOMI inputs on the TCOH product, we individually swapped each TROPOMI input into the OMI/MOPITT/AIRS product, replacing the corresponding input from Table 1. We then determined the difference in TCOH from the OMI/MOPITT/AIRS product that does not include TROPOMI. While this method will not yield the exact contribution from a particular retrieval because of the non-linear nature of OH chemistry, it does yield information about the relative importance of each species. Swapping in TROPOMI CO, H₂O_(v), and O₃ changed TCOH by less than 2%, while using TROPOMI HCHO increased TCOH by 3%. In contrast, TROPOMI NO₂ increased TCOH by 29%, showing that the high bias in the TROPOMI TCOH product is dominated by differences in NO₂.

The increased TCOH in the TROPOMI product likely results from a combination of differences in the NO₂ retrieval algorithm as well as instrumental differences. Comparison of the KNMI and MINDS retrievals illustrate this point. When compared to OMI, the MINDS NO₂ retrieval has a NMB of 58% for May 2018, as compared to a NMB of 145% for the KNMI retrieval. The closer agreement is unsurprising since the MINDS NO₂ uses the same retrieval algorithm as for OMI. Substituting the MINDS NO₂ as an input to the TROPOMI product (TROPOMI-MINDS product) reduces the bias with respect to the OMI/MOPITT/AIRS product to 18% (Fig. S12). While this is an improvement in agreement, the differences in TCOH as well as the lack of change in r^2 value still suggest that differences between OMI and TROPOMI unrelated to the retrieval algorithm account for some of the discrepancy.



The results here demonstrate the sensitivity of the methodology to any systematic bias in the input retrievals. As with the random error analysis, the level of uncertainty introduced by these biases is low enough to allow for a meaningful OH product. Despite these differences, the methodology to determine TCOH using machine learning that we have presented here still captures the variability in TCOH, consistent with the ATom evaluation outlined in Section 5.1. To reduce the uncertainty of TCOH, better evaluation of NO₂ in the remote atmosphere is needed to determine which retrievals, if any, are accurate.

6 Discussion and recommendations for future observations

The method of estimating clear-sky TCOH presented here has the potential to increase our understanding of the atmospheric oxidation capacity. Because of the long record of observations from MOPITT, OMI, AIRS, and MODIS, we can calculate tropical TCOH from 2005 to the present, and since the methodology is not constrained to a particular satellite, newer satellite missions could extend the dataset beyond the end of these instruments' lifetimes. In addition, this methodology will provide sub-hemispheric information on OH variability, supplementing information available from MCF inversions.

The methodology could be expanded to the extra-tropics and over land, allowing for global constraints on OH. This will likely require additional satellite retrievals, like that of isoprene (Wells et al., 2020), in regions with more complex VOC chemistry than in the remote atmosphere. Expanding this product beyond the tropics could increase understanding of global CH₄, CO, and VOC trends and variability and allow for a wider range of satellite retrievals as inputs. For example, geostationary air quality satellites such as TEMPO (Tropospheric Emissions: Monitoring of Pollution), scheduled to be launched in 2023, will provide retrievals of most of the necessary inputs to the machine learning model, allowing for the understanding of diurnal variability in TCOH and potentially in the diurnal variability of ozone production (Zhu et al., 2022b).

A similar methodology could likely be used to determine OH at different layers of the atmosphere. Because CH₄ loss is not evenly distributed throughout the tropospheric column, vertically resolved OH would better help inform this process. While column inputs, such as those discussed here, could be used, the inclusion of vertically resolved satellite retrievals, such as the AIRS H₂O_(v) layers, would provide additional information. Tropospheric O₃ at different atmospheric layers, such as that previously provided by the TES satellite, could also be invaluable here, as O₃ is a large driver of primary OH production.

Satellite-derived OH would also provide a much-needed, observational constraint on OH variability in global chemistry models. Because the methodology can capture variability in TCOH of both observations and 3-dimensional model output, TCOH trends from a satellite-constrained product could be used to evaluate modeled trends and as well as the spatial variability resulting from events like ENSO. While the satellite-derived OH could not explicitly indicate the cause of differences, the spatial distribution of the differences as well as differences in observed and modeled machine learning model inputs could indicate potential dynamical or emission sources of error in the 3D model.

Further, the combination of the satellite-derived OH and the machine learning model could help identify the impacts of any diagnosed errors in emissions inventories as well as the impacts of unexpected events, such as COVID-19-related shutdowns, on TCOH. For example, if there are significant discrepancies between observed and modeled NO₂ in a specific region of the atmosphere, the satellite NO₂ could be scaled to more closely match the 3D model values and then be input into the machine



learning model. The difference in TCOH would then indicate the relative impact of the model error, serving as a computationally efficient way to identify the impacts of these errors on the atmospheric oxidation capacity. A similar methodology could be used for unexpected events that significantly impact emissions of OH drivers, allowing for quick determination of their potential impacts on the atmospheric oxidation capacity before emissions inventories could be revised.

While we have shown that the methodology captures the variability of OH, it is unclear whether a bias in magnitude when compared to observations of OH results from GBRT model deficiencies or structural differences between the *in situ* observations and the training dataset. Additional field campaigns with observations of OH and the GBRT model inputs would allow for a more thorough evaluation of both the OH product and the methodology itself. Such a field campaign would need to provide complete tropospheric columns of all species and cover less horizontal distance than the ATom profiles (e.g. from spiral flight patterns). *In situ* observations of NO₂ without significant interference from NO_x reservoir species are also needed to reduce uncertainty. Alternatively, NO₂ and other species could be measured through aircraft-based remote sensing. Finally, repeated sampling over the same locations for multiple days within a defined area would allow for meaningful statistical analysis while also allowing for the comparison of TCOH columns calculated from satellite observations.

Finally, accuracy of the TCOH product is dependent on the accuracy of the satellite retrievals input into the machine learning model, with the NO₂ retrieval having the largest effect. To reduce the uncertainty of the TCOH product, more information about the accuracy of individual NO₂ retrievals is required. Currently, there is little validation of OMI and TROPOMI NO₂ retrievals in the remote, tropical atmosphere, so it is difficult to assess, which retrievals, if any, are correct. Even retrievals of TROPOMI and OMI made with the same algorithm show differences, suggesting that instrumental differences could also affect the results. Future satellite missions should focus on trying to reduce the uncertainty in NO₂ retrievals, both through improvements in instrument design and algorithm development.

7 Data Availability

Output from the MERRA2 GMI simulation are publicly available at <https://acd-ext.gsfc.nasa.gov/Projects/GEOSCCM/MERRA2GMI/> (NASA Goddard Space Flight Center, 2022). All satellite products, except for TROPOMI water vapor, are available at <https://disc.gsfc.nasa.gov/GESDISC> (2022). Data from the ATom campaign are located at <https://daac.ornl.gov> (Wofsy et al., 2021).

8 Author contributions

DCA wrote the manuscript, performed the data analysis, and created the GBRT model. DCA, BND, JMN, and MBFC developed the idea for the methodology. SAS performed three-dimensional modeling for the work. JMN provided advice on machine learning. JL helped perform data analysis. All authors helped develop ideas for the analysis and contributed to the manuscript.

9 Competing Interests

BND is a member of the editorial board of Atmospheric Chemistry and Physics. The peer-review process was guided by an independent editor, and the authors also have no other competing interests to declare.

10 Financial support

This research has been supported by the National Aeronautics and Space Administration (NASA) Atmospheric Composition Campaign Data Analysis and Modeling (ACCDAM) program (grant no. 80NSSC21K1440).



756

757 **11 Acknowledgements**

758 The authors wish to thank Lok Chan and Diego Loyola for use of the TROPOMI water vapor product.

759

760 **12 References**

761

762 Anderson, D. C., Nicely, J. M., Salawitch, R. J., Canty, T. P., Dickerson, R. R., Hanisco, T. F., Wolfe, G. M.,
 763 Apel, E. C., Atlas, E., Bannan, T., Bauguitte, S., Blake, N. J., Bresch, J. F., Campos, T. L., Carpenter, L. J.,
 764 Cohen, M. D., Evans, M., Fernandez, R. P., Kahn, B. H., Kinnison, D. E., Hall, S. R., Harris, N. R., Hornbrook,
 765 R. S., Lamarque, J. F., Le Breton, M., Lee, J. D., Percival, C., Pfister, L., Pierce, R. B., Riemer, D. D., Saiz-
 766 Lopez, A., Stunder, B. J., Thompson, A. M., Ullmann, K., Vaughan, A., and Weinheimer, A. J.: A pervasive
 767 role for biomass burning in tropical high ozone/low water structures, *Nat Commun*, 7, 10267,
 768 <https://doi.org/10.1038/ncomms10267>, 2016.

769 Anderson, D. C., Duncan, B. N., Fiore, A. M., Baublitz, C. B., Follette-Cook, M. B., Nicely, J. M., and Wolfe,
 770 G. M.: Spatial and temporal variability in the hydroxyl (OH) radical: understanding the role of large-scale
 771 climate features and their influence on OH through its dynamical and photochemical drivers,
 772 *Atmospheric Chemistry and Physics*, 21, 6481-6508, <https://doi.org/10.5194/acp-21-6481-2021>, 2021.

773 Anderson, D. C., Follette-Cook, M. B., Strode, S. A., Nicely, J. M., Liu, J., Ivatt, P. D., and Duncan, B. N.: A
 774 machine learning methodology for the generation of a parameterization of the hydroxyl radical, *Geosci.*
 775 *Model Dev.*, 15, 6341-6358, <https://doi.org/10.5194/gmd-15-6341-2022>, 2022.

776 Bedka, S., Knuteson, R., Revercomb, H., Tobin, D., and Turner, D.: An assessment of the absolute
 777 accuracy of the Atmospheric Infrared Sounder v5 precipitable water vapor product at tropical,
 778 midlatitude, and arctic ground-truth sites: September 2002 through August 2008, *Journal of Geophysical*
 779 *Research: Atmospheres*, 115, D17310, <https://doi.org/10.1029/2009JD013139>, 2010.

780 Borsdorff, T., aan de Brugh, J., Schneider, A., Lorente, A., Birk, M., Wagner, G., Kivi, R., Hase, F., Feist, D.
 781 G., Sussmann, R., Rettinger, M., Wunch, D., Warneke, T., and Landgraf, J.: Improving the TROPOMI CO
 782 data product: update of the spectroscopic database and destripping of single orbits, *Atmos. Meas. Tech.*,
 783 12, 5443-5455, <https://doi.org/10.5194/amt-12-5443-2019>, 2019.

784 Brune, W. H., Miller, D. O., Thames, A. B., Allen, H. M., Apel, E. C., Blake, D. R., Bui, T. P., Commane, R.,
 785 Crounse, J. D., Daube, B. C., Diskin, G. S., DiGangi, J. P., Elkins, J. W., Hall, S. R., Hanisco, T. F., Hannun, R.
 786 A., Hints, E. J., Hornbrook, R. S., Kim, M. J., McKain, K., Moore, F. L., Neuman, J. A., Nicely, J. M., Peischl,
 787 J., Ryerson, T. B., St. Clair, J. M., Sweeney, C., Teng, A. P., Thompson, C., Ullmann, K., Veres, P. R.,
 788 Wennberg, P. O., and Wolfe, G. M.: Exploring Oxidation in the Remote Free Troposphere: Insights From
 789 Atmospheric Tomography (ATom), *Journal of Geophysical Research: Atmospheres*, 125, e2019JD031685,
 790 <https://doi.org/10.1029/2019jd031685>, 2020.

791 Buchholz, R. R., Deeter, M. N., Worden, H. M., Gille, J., Edwards, D. P., Hannigan, J. W., Jones, N. B.,
 792 Paton-Walsh, C., Griffith, D. W. T., Smale, D., Robinson, J., Strong, K., Conway, S., Sussmann, R., Hase, F.,
 793 Blumenstock, T., Mahieu, E., and Langerock, B.: Validation of MOPITT carbon monoxide using ground-
 794 based Fourier transform infrared spectrometer data from NDACC, *Atmos. Meas. Tech.*, 10, 1927-1956,
 795 <https://doi.org/10.5194/amt-10-1927-2017>, 2017.



- 796 Burnett, C. R., and Minschwaner, K.: Continuing development in the regime of decreased atmospheric
 797 column OH at Fritz Peak, Colorado, Geophysical Research Letters, 25, 1313-1316,
 798 <https://doi.org/10.1029/98GL01062>, 1998.
- 799 Chan, K. L., Xu, J., Slijkhuis, S., Valks, P., and Loyola, D.: TROPOspheric Monitoring Instrument
 800 observations of total column water vapour: Algorithm and validation, Science of The Total Environment,
 801 821, 153232, <https://doi.org/10.1016/j.scitotenv.2022.153232>, 2022.
- 802 Chen, T., and Guestrin, C.: XGBoost: A Scalable Tree Boosting System, KDD '16: Proceedings of the 22nd
 803 ACM SIGKDD International Conference on Knowledge Discovery and Data Mining, 13 - 17 Aug. 2016,
 804 785-794, San Francisco, CA, USA, <https://doi.org/10.1145/2939672.2939785>, 2016.
- 805 Chin, T. M., Vazquez-Cuervo, J., and Armstrong, E. M.: A multi-scale high-resolution analysis of global sea
 806 surface temperature, Remote Sensing of Environment, 200, 154-169,
 807 <https://doi.org/10.1016/j.rse.2017.07.029>, 2017.
- 808 Choi, S., Lamsal, L. N., Follette-Cook, M., Joiner, J., Krotkov, N. A., Swartz, W. H., Pickering, K. E.,
 809 Loughner, C. P., Appel, W., Pfister, G., Saide, P. E., Cohen, R. C., Weinheimer, A. J., and Herman, J. R.:
 810 Assessment of NO₂ observations during DISCOVER-AQ and KORUS-AQ field campaigns, Atmos. Meas.
 811 Tech., 13, 2523-2546, <https://10.5194/amt-13-2523-2020>, 2020.
- 812 De Smedt, I., Theys, N., Yu, H., Danckaert, T., Lerot, C., Compernelle, S., Van Roozendaal, M., Richter, A.,
 813 Hilboll, A., Peters, E., Pedernana, M., Loyola, D., Beirle, S., Wagner, T., Eskes, H., van Geffen, J.,
 814 Boersma, K. F., and Veefkind, P.: Algorithm theoretical baseline for formaldehyde retrievals from S5P
 815 TROPOMI and from the QA4ECV project, Atmospheric Measurement Techniques, 11, 2395-2426,
 816 <https://10.5194/amt-11-2395-2018>, 2018.
- 817 De Smedt, I., Pinardi, G., Vigouroux, C., Compernelle, S., Bais, A., Benavent, N., Boersma, F., Chan, K. L.,
 818 Donner, S., Eichmann, K. U., Hedelt, P., Hendrick, F., Irie, H., Kumar, V., Lambert, J. C., Langerock, B.,
 819 Lerot, C., Liu, C., Loyola, D., PETERS, A., Richter, A., Rivera Cárdenas, C., Romahn, F., Ryan, R. G., Sinha, V.,
 820 Theys, N., Vlietinck, J., Wagner, T., Wang, T., Yu, H., and Van Roozendaal, M.: Comparative assessment
 821 of TROPOMI and OMI formaldehyde observations and validation against MAX-DOAS network column
 822 measurements, Atmos. Chem. Phys., 21, 12561-12593, <https://10.5194/acp-21-12561-2021>, 2021.
- 823 Deeter, M. N., Edwards, D. P., Francis, G. L., Gille, J. C., Mao, D., Martínez-Alonso, S., Worden, H. M.,
 824 Ziskin, D., and Andreae, M. O.: Radiance-based retrieval bias mitigation for the MOPITT instrument: the
 825 version 8 product, Atmospheric Measurement Techniques, 12, 4561-4580, [https://10.5194/amt-12-](https://10.5194/amt-12-4561-2019)
 826 4561-2019, 2019.
- 827 Duncan, B., Portman, D., Bey, I., and Spivakovsky, C.: Parameterization of OH for efficient computation in
 828 chemical tracer models, Journal of Geophysical Research: Atmospheres, 105, 12259-12262,
 829 <https://10.1029/1999JD901141>, 2000.
- 830 Duncan, B. N., Strahan, S. E., Yoshida, Y., Steenrod, S. D., and Livesey, N.: Model study of the cross-
 831 tropopause transport of biomass burning pollution, Atmos. Chem. Phys., 7, 3713-3736, [10.5194/acp-7-](https://10.5194/acp-7-3713-2007)
 832 3713-2007, 2007.
- 833 Elith, J., Leathwick, J. R., and Hastie, T.: A working guide to boosted regression trees, J Anim Ecol, 77,
 834 802-813, <https://10.1111/j.1365-2656.2008.01390.x>, 2008.



- 835 Garane, K., Koukouli, M. E., Verhoelst, T., Lerot, C., Heue, K. P., Fioletov, V., Balis, D., Bais, A., Bazureau,
 836 A., Dehn, A., Goutail, F., Granville, J., Griffin, D., Hubert, D., Keppens, A., Lambert, J. C., Loyola, D.,
 837 McLinden, C., Pazmino, A., Pommereau, J. P., Redondas, A., Romahn, F., Valks, P., Van Roozendael, M.,
 838 Xu, J., Zehner, C., Zerefos, C., and Zimmer, W.: TROPOMI/S5P total ozone column data: global ground-
 839 based validation and consistency with other satellite missions, *Atmos. Meas. Tech.*, 12, 5263-5287,
 840 <https://10.5194/amt-12-5263-2019>, 2019.
- 841 Gelaro, R., McCarty, W., Suarez, M. J., Todling, R., Molod, A., Takacs, L., Randles, C., Darmenov, A.,
 842 Bosilovich, M. G., Reichle, R., Wargan, K., Coy, L., Cullather, R., Draper, C., Akella, S., Buchard, V., Conaty,
 843 A., da Silva, A., Gu, W., Kim, G. K., Koster, R., Lucchesi, R., Merkova, D., Nielsen, J. E., Partyka, G.,
 844 Pawson, S., Putman, W., Rienecker, M., Schubert, S. D., Sienkiewicz, M., and Zhao, B.: The Modern-Era
 845 Retrospective Analysis for Research and Applications, Version 2 (MERRA-2), *J Clim*, Volume 30, 5419-
 846 5454, <https://10.1175/JCLI-D-16-0758.1>, 2017.
- 847 GES DISC: Earth Science Data at NASA, available at <https://disc.gsfc.nasa.gov>, last access: 1 Nov. 2022.
- 848 González Abad, G., Liu, X., Chance, K., Wang, H., Kurosu, T. P., and Suleiman, R.: Updated Smithsonian
 849 Astrophysical Observatory Ozone Monitoring Instrument (SAO OMI) formaldehyde retrieval,
 850 *Atmospheric Measurement Techniques*, 8, 19-32, <https://10.5194/amt-8-19-2015>, 2015.
- 851 González Abad, G., Vasilkov, A., Seftor, C., Liu, X., and Chance, K.: Smithsonian Astrophysical Observatory
 852 Ozone Mapping and Profiler Suite (SAO OMPS) formaldehyde retrieval, *Atmospheric Measurement*
 853 *Techniques*, 9, 2797-2812, <https://10.5194/amt-9-2797-2016>, 2016.
- 854 Hedelius, J. K., He, T. L., Jones, D. B. A., Baier, B. C., Buchholz, R. R., De Mazière, M., Deutscher, N. M.,
 855 Dubey, M. K., Feist, D. G., Griffith, D. W. T., Hase, F., Iraci, L. T., Jeseck, P., Kiel, M., Kivi, R., Liu, C.,
 856 Morino, I., Notholt, J., Oh, Y. S., Ohyama, H., Pollard, D. F., Rettinger, M., Roche, S., Roehl, C. M.,
 857 Schneider, M., Shiomi, K., Strong, K., Sussmann, R., Sweeney, C., Té, Y., Uchino, O., Velazco, V. A., Wang,
 858 W., Warneke, T., Wennberg, P. O., Worden, H. M., and Wunch, D.: Evaluation of MOPITT Version 7 joint
 859 TIR–NIR XCO retrievals with TCCON, *Atmos. Meas. Tech.*, 12, 5547-5572, [https://10.5194/amt-12-5547-](https://10.5194/amt-12-5547-2019)
 860 2019, 2019.
- 861 Ivatt, P. D., and Evans, M. J.: Improving the prediction of an atmospheric chemistry transport model
 862 using gradient-boosted regression trees, *Atmospheric Chemistry and Physics*, 20, 8063-8082,
 863 <https://10.5194/acp-20-8063-2020>, 2020.
- 864 Keller, C. A., and Evans, M. J.: Application of random forest regression to the calculation of gas-phase
 865 chemistry within the GEOS-Chem chemistry model v10, *Geoscientific Model Development*, 12, 1209-
 866 1225, <https://10.5194/gmd-12-1209-2019>, 2019.
- 867 Kelp, M. M., Jacob, D. J., Kutz, J. N., Marshall, J. D., and Tessum, C. W.: Toward Stable, General Machine-
 868 Learned Models of the Atmospheric Chemical System, *Journal of Geophysical Research: Atmospheres*,
 869 125, e2020JD032759, <https://doi.org/10.1029/2020JD032759>, 2020.
- 870 Labow, G. J., McPeters, R. D., Bhartia, P. K., and Kramarova, N.: A comparison of 40 years of SBUV
 871 measurements of column ozone with data from the Dobson/Brewer network, *Journal of Geophysical*
 872 *Research: Atmospheres*, 118, 7370-7378, <https://doi.org/10.1002/jgrd.50503>, 2013.



- 873 Lamsal, L. N., Krotkov, N. A., Celarier, E. A., Swartz, W. H., Pickering, K. E., Bucsela, E. J., Gleason, J. F.,
874 Martin, R. V., Philip, S., Irie, H., Cede, A., Herman, J., Weinheimer, A., Szykman, J. J., and Knepp, T. N.:
875 Evaluation of OMI operational standard NO₂ column retrievals using in situ and surface-based NO₂
876 observations, *Atmospheric Chemistry and Physics*, 14, 11587–11609, [https://doi.org/10.5194/acp-14-11587-](https://doi.org/10.5194/acp-14-11587-2014)
877 2014, 2014.
- 878 Lamsal, L. N., Krotkov, N. A., Vasilkov, A., Marchenko, S., Qin, W., Yang, E. S., Fasnacht, Z., Joiner, J., Choi,
879 S., Haffner, D., Swartz, W. H., Fisher, B., and Bucsela, E.: Ozone Monitoring Instrument (OMI) Aura
880 nitrogen dioxide standard product version 4.0 with improved surface and cloud treatments, *Atmos.*
881 *Meas. Tech.*, 14, 455–479, <https://doi.org/10.5194/amt-14-455-2021>, 2021.
- 882 Lamsal, L. N., Krotkov, N. A., Marchenko, S. V., Joiner, J., Oman, L., Vasilkov, A., Fisher, B., Qin, W., Yang,
883 E.-S., Fasnacht, Z., Choi, S., Leonard, P., and Haffner, D.: TROPOMI/S5P NO₂ Tropospheric, Stratospheric
884 and Total Columns MINDS 1-Orbit L2 Swath 5.5 km x 3.5 km, in, *NASA Goddard Earth Sciences Data and*
885 *Information Services Center (GES DISC) [data set]*, <https://doi.org/10.5067/MEASURES/MINDS/Data203>, 2022.
- 886 Laughner, J. L., Neu, J. L., Schimel, D., Wennberg, P. O., Barsanti, K., Bowman, K. W., Chatterjee, A.,
887 Croes, B. E., Fitzmaurice, H. L., Henze, D. K., Kim, J., Kort, E. A., Liu, Z., Miyazaki, K., Turner, A. J.,
888 Anenberg, S., Avise, J., Cao, H., Crisp, D., de Gouw, J., Eldering, A., Fyfe, J. C., Goldberg, D. L., Gurney, K.
889 R., Hasheminassab, S., Hopkins, F., Ivey, C. E., Jones, D. B. A., Liu, J., Lovenduski, N. S., Martin, R. V.,
890 McKinley, G. A., Ott, L., Poulter, B., Ru, M., Sander, S. P., Swart, N., Yung, Y. L., and Zeng, Z. C.: Societal
891 shifts due to COVID-19 reveal large-scale complexities and feedbacks between atmospheric chemistry
892 and climate change, *Proc Natl Acad Sci U S A*, 118, e2109481118, <https://doi.org/10.1073/pnas.2109481118>,
893 2021.
- 894 Levy, R. C., Mattoo, S., Munchak, L. A., Remer, L. A., Sayer, A. M., Patadia, F., and Hsu, N. C.: The
895 Collection 6 MODIS aerosol products over land and ocean, *Atmos. Meas. Tech.*, 6, 2989–3034,
896 <https://doi.org/10.5194/amt-6-2989-2013>, 2013.
- 897 Liang, Q., Chipperfield, M. P., Fleming, E. L., Abraham, N. L., Braesicke, P., Burkholder, J. B., Daniel, J. S.,
898 Dhomse, S., Fraser, P. J., Hardiman, S. C., Jackman, C. H., Kinnison, D. E., Krummel, P. B., Montzka, S. A.,
899 Morgenstern, O., McCulloch, A., Mühle, J., Newman, P. A., Orkin, V. L., Pitari, G., Prinn, R. G., Rigby, M.,
900 Rozanov, E., Stenke, A., Tummon, F., Velders, G. J. M., Visioni, D., and Weiss, R. F.: Deriving Global OH
901 Abundance and Atmospheric Lifetimes for Long-Lived Gases: A Search for CH₃CCl₃ Alternatives, *Journal*
902 *of Geophysical Research: Atmospheres*, 122, 11,914–11,933, <https://doi.org/10.1002/2017JD026926>, 2017.
- 903 Lovelock, J. E.: Methyl chloroform in the troposphere as an indicator of OH radical abundance, *Nature*,
904 267, 32–32, <https://doi.org/10.1038/267032a0>, 1977.
- 905 Mao, J., Ren, X., Brune, W. H., Olson, J. R., Crawford, J. H., Fried, A., Huey, L. G., Cohen, R. C., Heikes, B.,
906 Singh, H. B., Blake, D. R., Sachse, G. W., Diskin, G. S., Hall, S. R., and Shetter, R. E.: Airborne measurement
907 of OH reactivity during INTEX-B, *Atmos. Chem. Phys.*, 9, 163–173, <https://doi.org/10.5194/acp-9-163-2009>, 2009.
- 908 Martínez-Alonso, S., Deeter, M., Worden, H., Borsdorff, T., Aben, I., Commane, R., Daube, B., Francis, G.,
909 George, M., Landgraf, J., Mao, D., McKain, K., and Wofsy, S.: 1.5 years of TROPOMI CO measurements:
910 comparisons to MOPITT and ATom, *Atmos. Meas. Tech.*, 13, 4841–4864, [https://doi.org/10.5194/amt-13-4841-](https://doi.org/10.5194/amt-13-4841-2020)
911 2020, 2020.



- 912 McPeters, R. D., Frith, S., and Labow, G. J.: OMI total column ozone: extending the long-term data
 913 record, *Atmos. Meas. Tech.*, 8, 4845-4850, [https://10.5194/amt-8-4845-2015](https://doi.org/10.5194/amt-8-4845-2015), 2015.
- 914 Miller, D. O., and Brune, W. H.: Investigating the Understanding of Oxidation Chemistry Using 20 Years
 915 of Airborne OH and HO₂ Observations, *Journal of Geophysical Research: Atmospheres*, 127,
 916 e2021JD035368, <https://doi.org/10.1029/2021JD035368>, 2022.
- 917 Montzka, S. A., Krol, M., Dlugokencky, E., Hall, B., Jockel, P., and Lelieveld, J.: Small Interannual
 918 Variability of Global Atmospheric Hydroxyl, *Science*, 331, 67-69, [https://10.1126/science.1197640](https://doi.org/10.1126/science.1197640), 2011.
- 919 Murray, L. T., Mickley, L. J., Kaplan, J. O., Sofen, E. D., Pfeiffer, M., and Alexander, B.: Factors controlling
 920 variability in the oxidative capacity of the troposphere since the Last Glacial Maximum, *Atmospheric
 921 Chemistry and Physics*, 14, 3589-3622, [https://10.5194/acp-14-3589-2014](https://doi.org/10.5194/acp-14-3589-2014), 2014.
- 922 Murray, L. T., Fiore, A. M., Shindell, D. T., Naik, V., and Horowitz, L. W.: Large uncertainties in global
 923 hydroxyl projections tied to fate of reactive nitrogen and carbon, *Proceedings of the National Academy
 924 of Sciences*, 118, e2115204118, [https://10.1073/pnas.2115204118](https://doi.org/10.1073/pnas.2115204118), 2021.
- 925 NASA Goddard Space Flight Center. MERRA2 GMI, NASA [data set], [https://acd-
 926 ext.gsfc.nasa.gov/Projects/GEOSSCM/MERRA2GMI/](https://acd-ext.gsfc.nasa.gov/Projects/GEOSSCM/MERRA2GMI/), last access: 1 November 2022.
- 927 Naus, S., Montzka, S. A., Pandey, S., Basu, S., Dlugokencky, E. J., and Krol, M.: Constraints and biases in a
 928 tropospheric two-box model of OH, *Atmos. Chem. Phys.*, 19, 407-424, [https://10.5194/acp-19-407-2019](https://doi.org/10.5194/acp-19-407-2019),
 929 2019.
- 930 Nicely, J. M., Anderson, D. C., Canty, T. P., Salawitch, R. J., Wolfe, G. M., Apel, E. C., Arnold, S. R., Atlas, E.
 931 L., Blake, N. J., Bresch, J. F., Campos, T. L., Fernandez, R. P., Flemming, J., Hall, S. R., Hanisco, T. F.,
 932 Honomichl, S. B., Hornbrook, R. S., Huijnen, V., Kaser, L., Kinnison, D. E., Pan, L. L., Riemer, D. D., Saiz-
 933 Lopez, A., Steenrod, S. D., Stell, M. H., Tilmes, S., Turquety, S., Ullmann, K., and Weinheimer, A. J.: An
 934 observationally constrained evaluation of the oxidative capacity in the tropical western Pacific
 935 troposphere, *Journal of Geophysical Research: Atmospheres*, 121, 7461-7488,
 936 [https://10.1002/2016JD025067](https://doi.org/10.1002/2016JD025067), 2016.
- 937 Nicely, J. M., Salawitch, R. J., Canty, T., Anderson, D. C., Arnold, S. R., Chipperfield, M. P., Emmons, L. K.,
 938 Flemming, J., Huijnen, V., Kinnison, D. E., Lamarque, J.-F., Mao, J., Monks, S. A., Steenrod, S. D., Tilmes,
 939 S., and Turquety, S.: Quantifying the causes of differences in tropospheric OH within global models,
 940 *Journal of Geophysical Research: Atmospheres*, JD026239, [https://10.1002/2016JD026239](https://doi.org/10.1002/2016JD026239), 2017.
- 941 Nicely, J. M., Duncan, B. N., Hanisco, T. F., Wolfe, G. M., Salawitch, R. J., Deushi, M., Haslerud, A. S.,
 942 Jöckel, P., Josse, B., Kinnison, D. E., Klekociuk, A., Manyin, M. E., Marécal, V., Morgenstern, O., Murray, L.
 943 T., Myhre, G., Oman, L. D., Pitari, G., Pozzer, A., Quaglia, I., Revell, L. E., Rozanov, E., Stenke, A., Stone, K.,
 944 Strahan, S., Tilmes, S., Tost, H., Westervelt, D. M., and Zeng, G.: A machine learning examination of
 945 hydroxyl radical differences among model simulations for CCMI-1, *Atmospheric Chemistry and Physics*,
 946 20, 1341-1361, [https://10.5194/acp-20-1341-2020](https://doi.org/10.5194/acp-20-1341-2020), 2020.
- 947 Oman, L. D., Douglass, A. R., Ziemke, J. R., Rodriguez, J. M., Waugh, D. W., and Nielsen, J. E.: The ozone
 948 response to ENSO in Aura satellite measurements and a chemistry-climate simulation, *Journal of
 949 Geophysical Research-Atmospheres*, 118, 965-976, [https://10.1029/2012jd018546](https://doi.org/10.1029/2012jd018546), 2013.



- 950 Orbe, C., Oman, L. D., Strahan, S. E., Waugh, D. W., Pawson, S., Takacs, L. L., and Molod, A. M.: Large-
 951 Scale Atmospheric Transport in GEOS Replay Simulations, *Journal of Advances in Modeling Earth*
 952 *Systems*, 9, 2545-2560, 10.1002/2017ms001053, 2017.
- 953 Pérez-Ramírez, D., Smirnov, A., Pinker, R. T., Petrenko, M., Román, R., Chen, W., Ichoku, C., Noël, S.,
 954 Abad, G. G., Lyamani, H., and Holben, B. N.: Precipitable water vapor over oceans from the Maritime
 955 Aerosol Network: Evaluation of global models and satellite products under clear sky conditions,
 956 *Atmospheric Research*, 215, 294-304, <https://doi.org/10.1016/j.atmosres.2018.09.007>, 2019.
- 957 Pickett, H. M., Drouin, B. J., Canty, T., Salawitch, R. J., Fuller, R. A., Perun, V. S., Livesey, N. J., Waters, J.
 958 W., Stachnik, R. A., Sander, S. P., Traub, W. A., Jucks, K. W., and Minschwaner, K.: Validation of Aura
 959 Microwave Limb Sounder OH and HO₂ measurements, *Journal of Geophysical Research: Atmospheres*,
 960 113, D16S30, <https://doi.org/10.1029/2007JD008775>, 2008.
- 961 Pimlott, M. A., Pope, R. J., Kerridge, B. J., Latter, B. G., Knappett, D. S., Heard, D. E., Ventress, L. J.,
 962 Siddans, R., Feng, W., and Chipperfield, M. P.: Investigating the global OH radical distribution using
 963 steady-state approximations and satellite data, *Atmos. Chem. Phys.*, 22, 10467-10488,
 964 <https://10.5194/acp-22-10467-2022>, 2022.
- 965 Rigby, M., Montzka, S. A., Prinn, R. G., White, J. W. C., Young, D., O'Doherty, S., Lunt, M. F., Ganesan, A.
 966 L., Manning, A. J., Simmonds, P. G., Salameh, P. K., Harth, C. M., Muhle, J., Weiss, R. F., Fraser, P. J.,
 967 Steele, L. P., Krummel, P. B., McCulloch, A., and Park, S.: Role of atmospheric oxidation in recent
 968 methane growth, *Proc Natl Acad Sci USA*, 114, 5373-5377, <https://10.1073/pnas.1616426114>, 2017.
- 969 Shah, V., Jacob, D. J., Dang, R., Lamsal, L. N., Strode, S. A., Steenrod, S. D., et al. (2022). Nitrogen oxides
 970 in the free troposphere: Implications for tropospheric oxidants and the interpretation of satellite NO₂
 971 measurements. *EGUsphere*, 2022, 1-47. [https://egusphere.copernicus.org/preprints/egusphere-2022-](https://egusphere.copernicus.org/preprints/egusphere-2022-656/)
 972 [656/](https://egusphere.copernicus.org/preprints/egusphere-2022-656/).
- 973 Silvern, R. F., Jacob, D. J., Travis, K. R., Sherwen, T., Evans, M. J., Cohen, R. C., Laughner, J. L., Hall, S. R.,
 974 Ullmann, K., Crounse, J. D., Wennberg, P. O., Peischl, J., and Pollack, I. B.: Observed NO/NO₂ Ratios in the
 975 Upper Troposphere Imply Errors in NO-NO₂-O₃ Cycling Kinetics or an Unaccounted NO_x Reservoir,
 976 *Geophysical Research Letters*, 45, 4466-4474, <https://doi.org/10.1029/2018GL077728>, 2018.
- 977 Stauffer, R. M., Thompson, A. M., and Young, G. S.: Tropospheric ozonesonde profiles at long-term U.S.
 978 monitoring sites: 1. A climatology based on self-organizing maps, *Journal of Geophysical Research:*
 979 *Atmospheres*, 121, 1320-1339, <https://doi.org/10.1002/2015JD023641>, 2016.
- 980 Strahan, S. E., Duncan, B. N., and Hoor, P.: Observationally derived transport diagnostics for the
 981 lowermost stratosphere and their application to the GMI chemistry and transport model, *Atmos. Chem.*
 982 *Phys.*, 7, 2435-2445, <https://10.5194/acp-7-2435-2007>, 2007.
- 983 Strode, S. A., Ziemke, J. R., Oman, L. D., Lamsal, L. N., Olsen, M. A., and Liu, J.: Global changes in the
 984 diurnal cycle of surface ozone, *Atmospheric Environment*, 199, 323-333,
 985 <https://10.1016/j.atmosenv.2018.11.028>, 2019.
- 986 Susskind, J., Blaisdell, J. M., and Iredell, L.: Improved methodology for surface and atmospheric
 987 soundings, error estimates, and quality control procedures: the atmospheric infrared sounder science



- 988 team version-6 retrieval algorithm, *Journal of Applied Remote Sensing*, 8, 084994,
 989 <https://10.1117/1.Jrs.8.084994>, 2014.
- 990 Thompson, C. R., Wofsy, S. C., Prather, M. J., Newman, P. A., Hanisco, T. F., Ryerson, T. B., Fahey, D. W.,
 991 Apel, E. C., Brock, C. A., Brune, W. H., Froyd, K., Katich, J. M., Nicely, J. M., Peischl, J., Ray, E., Veres, P. R.,
 992 Wang, S., Allen, H. M., Asher, E., Bian, H., Blake, D., Bourgeois, I., Budney, J., Bui, T. P., Butler, A.,
 993 Campuzano-Jost, P., Chang, C., Chin, M., Commane, R., Correa, G., Crounse, J. D., Daube, B., Dibb, J. E.,
 994 DiGangi, J. P., Diskin, G. S., Dollner, M., Elkins, J. W., Fiore, A. M., Flynn, C. M., Guo, H., Hall, S. R.,
 995 Hannun, R. A., Hills, A., Hints, E. J., Hodzic, A., Hornbrook, R. S., Huey, L. G., Jimenez, J. L., Keeling, R. F.,
 996 Kim, M. J., Kupc, A., Lacey, F., Lait, L. R., Lamarque, J.-F., Liu, J., McKain, K., Meinardi, S., Miller, D. O.,
 997 Montzka, S. A., Moore, F. L., Morgan, E. J., Murphy, D. M., Murray, L. T., Nault, B. A., Neuman, J. A.,
 998 Nguyen, L., Gonzalez, Y., Rollins, A., Rosenlof, K., Sargent, M., Schill, G., Schwarz, J. P., Clair, J. M. S.,
 999 Steenrod, S. D., Stephens, B. B., Strahan, S. E., Strode, S. A., Sweeney, C., Thames, A. B., Ullmann, K.,
 1000 Wagner, N., Weber, R., Weinzierl, B., Wennberg, P. O., Williamson, C. J., Wolfe, G. M., and Zeng, L.: The
 1001 NASA Atmospheric Tomography (ATom) Mission: Imaging the Chemistry of the Global Atmosphere,
 1002 *Bulletin of the American Meteorological Society*, 103, E761-E790, <https://10.1175/BAMS-D-20-0315.1>,
 1003 2022.
- 1004 Turner, A. J., Frankenberg, C., Wennberg, P. O., and Jacob, D. J.: Ambiguity in the causes for decadal
 1005 trends in atmospheric methane and hydroxyl, *Proceedings of the National Academy of Sciences*, 114,
 1006 5367, <https://10.1073/pnas.1616020114>, 2017.
- 1007 Turner, A. J., Fung, I., Naik, V., Horowitz, L. W., and Cohen, R. C.: Modulation of hydroxyl variability by
 1008 ENSO in the absence of external forcing, *Proc Natl Acad Sci U S A*, 115, 8931-8936,
 1009 <https://10.1073/pnas.1807532115>, 2018.
- 1010 van Geffen, J., Boersma, K. F., Eskes, H., Sneep, M., ter Linden, M., Zara, M., and Veefkind, J. P.: S5P
 1011 TROPOMI NO₂ slant column retrieval: method, stability, uncertainties and comparisons with OMI,
 1012 *Atmos. Meas. Tech.*, 13, 1315-1335, <https://10.5194/amt-13-1315-2020>, 2020.
- 1013 Veefkind, J. P., Aben, I., McMullan, K., Förster, H., de Vries, J., Otter, G., Claas, J., Eskes, H. J., de Haan, J.
 1014 F., Kleipool, Q., van Weele, M., Hasekamp, O., Hoogeveen, R., Landgraf, J., Snel, R., Tol, P., Ingmann, P.,
 1015 Voors, R., Kruizinga, B., Vink, R., Visser, H., and Levelt, P. F.: TROPOMI on the ESA Sentinel-5 Precursor: A
 1016 GMES mission for global observations of the atmospheric composition for climate, air quality and ozone
 1017 layer applications, *Remote Sensing of Environment*, 120, 70-83,
 1018 <https://doi.org/10.1016/j.rse.2011.09.027>, 2012.
- 1019 Voulgarakis, A., Naik, V., Lamarque, J. F., Shindell, D. T., Young, P. J., Prather, M. J., Wild, O., Field, R. D.,
 1020 Bergmann, D., Cameron-Smith, P., Cionni, I., Collins, W. J., Dalsøren, S. B., Doherty, R. M., Eyring, V.,
 1021 Faluvegi, G., Folberth, G. A., Horowitz, L. W., Josse, B., MacKenzie, I. A., Nagashima, T., Plummer, D. A.,
 1022 Righi, M., Rumbold, S. T., Stevenson, D. S., Strode, S. A., Sudo, K., Szopa, S., and Zeng, G.: Analysis of
 1023 present day and future OH and methane lifetime in the ACCMIP simulations, *Atmospheric Chemistry and*
 1024 *Physics*, 13, 2563-2587, <https://10.5194/acp-13-2563-2013>, 2013.
- 1025 Wang, P., Piters, A., van Geffen, J., Tuinder, O., Stammes, P., and Kinne, S.: Shipborne MAX-DOAS
 1026 measurements for validation of TROPOMI NO₂ products, *Atmos. Meas. Tech.*, 13, 1413-1426,
 1027 <https://10.5194/amt-13-1413-2020>, 2020.



- 1028 Wells, K. C., Millet, D. B., Payne, V. H., Deventer, M. J., Bates, K. H., de Gouw, J. A., Graus, M., Warneke,
 1029 C., Wisthaler, A., and Fuentes, J. D.: Satellite isoprene retrievals constrain emissions and atmospheric
 1030 oxidation, *Nature*, 585, 225–233, [https://10.1038/s41586-020-2664-3](https://doi.org/10.1038/s41586-020-2664-3), 2020.
- 1031 Wofsy, S. C., Afshar, S., Allen, H. M., Apel, E. C., Asher, E. C., Barletta, B., Bent, J., Bian, H., Biggs, B. C.,
 1032 Blake, D. R., Blake, N., Bourgeois, I., Brock, C. A., Brune, W. H., Budney, J. W., Bui, T. P., Butler, A.,
 1033 Campuzano-Jost, P., Chang, C. S., Chin, M., Commane, R., Correa, G., Crounse, J. D., Cullis, P. D., Daube,
 1034 B. C., Day, D. A., Dean-Day, J. M., Dibb, J. E., DiGangi, J. P., Diskin, G. S., Dollner, M., Elkins, J. W., Erdesz,
 1035 F., Fiore, A. M., Flynn, C. M., Froyd, K. D., Gesler, D. W., Hall, S. R., Hanisco, T. F., Hannun, R. A., Hills, A.
 1036 J., Hints, E. J., Hoffman, A., Hornbrook, R. S., Huey, L. G., Hughes, S., Jimenez, J. L., Johnson, B. J., Katich,
 1037 J. M., Keeling, R. F., Kim, M. J., Kupc, A., Lait, L. R., McKain, K., McLaughlin, R. J., Meinardi, S., Miller, D.
 1038 O., Montzka, S. A., Moore, F. L., Morgan, E. J., Murphy, D. M., Murray, L. T., Nault, B. A., Neuman, J. A.,
 1039 Newman, P. A., Nicely, J. M., Pan, X., Paplawsky, W., Peischl, J., Prather, M. J., Price, D. J., Ray, E. A.,
 1040 Reeves, J. M., Richardson, M., Rollins, A. W., Rosenlof, K. H., Ryerson, T. B., Scheuer, E., Schill, G. P.,
 1041 Schroder, J. C., Schwarz, J. P., St.Clair, J. M., Steenrod, S. D., Stephens, B. B., Strode, S. A., Sweeney, C.,
 1042 Tanner, D., Teng, A. P., Thames, A. B., Thompson, C. R., Ullmann, K., Veres, P. R., Wagner, N. L., Watt, A.,
 1043 Weber, R., Weinzierl, B. B., Wennberg, P. O., Williamson, C. J., Wilson, J. C., Wolfe, G. M., Woods, C. T.,
 1044 Zeng, L. H., and Vieznor, N.: ATom: Merged Atmospheric Chemistry, Trace Gases, and Aerosols, Version
 1045 2, in, ORNL Distributed Active Archive Center, 2021. [https://10.3334/ORNLDAAC/1925](https://doi.org/10.3334/ORNLDAAC/1925).
- 1046 Wolfe, G. M., Nicely, J. M., St Clair, J. M., Hanisco, T. F., Liao, J., Oman, L. D., Brune, W. B., Miller, D.,
 1047 Thames, A., Gonzalez Abad, G., Ryerson, T. B., Thompson, C. R., Peischl, J., McCain, K., Sweeney, C.,
 1048 Wennberg, P. O., Kim, M., Crounse, J. D., Hall, S. R., Ullmann, K., Diskin, G., Bui, P., Chang, C., and Dean-
 1049 Day, J.: Mapping hydroxyl variability throughout the global remote troposphere via synthesis of airborne
 1050 and satellite formaldehyde observations, *Proc Natl Acad Sci USA*, 116, 11171–11180,
 1051 [https://10.1073/pnas.1821661116](https://doi.org/10.1073/pnas.1821661116), 2019.
- 1052 Wolter, K., and Timlin, M. S.: El Niño/Southern Oscillation behaviour since 1871 as diagnosed in an
 1053 extended multivariate ENSO index (MEI.ext), *International Journal of Climatology*, 31, 1074–1087,
 1054 [https://10.1002/joc.2336](https://doi.org/10.1002/joc.2336), 2011.
- 1055 Zhao, Y., Saunio, M., Bousquet, P., Lin, X., Berchet, A., Hegglin, M. I., Canadell, J. G., Jackson, R. B.,
 1056 Hauglustaine, D. A., Szopa, S., Stavert, A. R., Abraham, N. L., Archibald, A. T., Bekki, S., Deushi, M., Jöckel,
 1057 P., Josse, B., Kinnison, D., Kirner, O., Maréchal, V., Connor, F. M., Plummer, D. A., Revell, L. E., Rozanov, E.,
 1058 Stenke, A., Strode, S., Tilmes, S., Dlugokencky, E. J., and Zheng, B.: Inter-model comparison of global
 1059 hydroxyl radical (OH) distributions and their impact on atmospheric methane over the 2000–2016
 1060 period, *Atmospheric Chemistry and Physics*, 19, 13701–13723, [10.5194/acp-19-13701-2019](https://doi.org/10.5194/acp-19-13701-2019), 2019.
- 1061 Zhu, L., Jacob, D. J., Kim, P. S., Fisher, J. A., Yu, K., Travis, K. R., Mickley, L. J., Yantosca, R. M., Sulprizio, M.
 1062 P., De Smedt, I., González Abad, G., Chance, K., Li, C., Ferrare, R., Fried, A., Hair, J. W., Hanisco, T. F.,
 1063 Richter, D., Jo Scarino, A., Walega, J., Weibring, P., and Wolfe, G. M.: Observing atmospheric
 1064 formaldehyde (HCHO) from space: validation and intercomparison of six retrievals from four satellites
 1065 (OMI, GOME2A, GOME2B, OMPS) with SEACRS aircraft observations over the southeast US, *Atmospheric*
 1066 *Chemistry and Physics*, 16, 13477–13490, [10.5194/acp-16-13477-2016](https://doi.org/10.5194/acp-16-13477-2016), 2016.
- 1067
 1068 Zhu, Q., Laughner, J. L., and Cohen, R. C.: Combining Machine Learning and Satellite Observations to
 1069 Predict Spatial and Temporal Variation of near Surface OH in North American Cities, *Environmental*
 1070 *Science & Technology*, 7362 – 7371, [https://10.1021/acs.est.1c05636](https://doi.org/10.1021/acs.est.1c05636), 2022a.



1071
1072 Zhu, Q., Laughner, J. L., and Cohen, R. C.: Estimate of OH trends over one decade in North American
1073 cities, Proc Natl Acad Sci U S A, 119, e2117399119, <https://doi.org/10.1073/pnas.2117399119>, 2022b.
1074
1075